Transport of zinc ions in the hyporheic zone: Experiments and simulations

Guangqiu Jin[1], Zhongtian Zhang[1], Ruzhong Li[2], Chen Chen[1], Hongwu Tang[1,#], Ling Li[3], D. A. Barry[4]

[1]State Key Laboratory of Hydrology-Water Resources and Hydraulic Engineering, Hohai University, Nanjing, China

Emails: jingq@hhu.edu.cn, zhongtian_zhang@163.com, hwtang@hhu.edu.cn，chenchenhhu@163.com

[2]School of Resources and Environmental Engineering, Hefei University of Technology, Hefei 230009, China

Emails:Lrz1970@163.com

[3]School of Engineering, Westlake University, Hangzhou, China

Email: liling@westlake.edu.cn

[4]Laboratoire de technologie écologique, Institut d'ingénierie de l'environnement, Faculté de l'environnement naturel, architectural et construit (ENAC), Ecole Polytechnique Fédérale de Lausanne (EPFL), Station 2, 1015 Lausanne, Switzerland

Email: andrew.barry@epfl.ch

[#]Author to whom all correspondence should be addressed. Tel: +86 (25) 8378-6662. Fax: +86 (25) 8373-5375

Abstract

Large amounts of toxic metals are discharged into rivers and lakes, but little is known about the factors that drive the adsorption and transformation of these metals in the hyporheic zone and the exchange flux across the sediment-water interface. To better understand transport and transformation of metal ions in the hyporheic zone, flume experiments and numerical simulations were performed in a streambed with periodic bedforms using zinc ions. Compared to non-adsorbing contaminant, the results show that adsorption leads to a more rapid decrease in the concentration of Zn^{2+} in the overlying water, and a lower final concentration is reached. The mass of adsorbed ions is several times higher than that of free ions in the bedform's water phase. Indeed, metal adsorption is in the shallow layer of the streambed. Although this prevents heavy metal groundwater contamination, the same cannot be said of shallow layer of the hyporheic zone. Knowledge of the migration and transformation of metal ions in the hyporheic zone provides insights pertinent to the restoration of polluted rivers.

Keywords: Metal ions; Zinc ions; Hyporheic exchange; Adsorption; Flume experiment; Numerical simulation

1. Introduction

Metals have been used by humans for thousands of years [1], and a large amount of metals are discharged from domestic [2,3] and industrial sources [4-6] into rivers and lakes [7,8]. It is noted that some of these metals, especially heavy metals [9-11], are driven by hydrodynamic forces [7,8,12]. They are transported and retained in aquatic and hyporheic ecosystems [13] for long periods as they are difficult to degrade [14,15]. These toxic metals may cause protein denaturation, enzyme inactivation and DNA damage [16,17] and thus pose a threat to aquatic ecosystems [18,19] and humans [20].

The hyporheic zone provides an area for surface water-groundwater exchange [21,22], transport and transformation of nutrients and trace metals [23,24] and is a habitat for aquatic biota [25,26]. It can act as a physical, chemical and biological filter to transform pollutants [27]. Notably, metallic pollutants are likely to be released back to the overlying water from the hyporheic zone under hydrodynamic forcing, thereby causing secondary pollution [28,29].

Manganese and iron oxides attached to sediments can increase the removal rate of trace metals and heavy metals as they may provide additional sites for adsorption [30,31]. *Fuller and Bargar* [32] investigated the distribution of zinc (Zn) and manganese oxides in Pinal Creek, Arizona, by field sampling and found attenuation of zinc is affected by biogenic manganese oxides in hyporheic zone. *Peña et al.* [33] found in their bacterial culture experiments that Ni could be effectively scavenged by bacterial biomass-birnessite assemblages. However, they mainly focused on the mechanism of metal adsorption-desorption rather than their transport in the hyporheic zone. *Ren and Packman* [34,35] conducted flume experiments to investigate the stream-streambed interface flux of dissolved Zn, Cu and phosphate in the presence of colloids, and found that adsorption had a significant effect on metal transport in the hyporheic zone. They examined the exchange rate of ions between stream and streambed, but did not consider the distribution pattern of ions in the streambed. *Palumbo-Roe et al.* [36, 37] investigated the sources of metals in the hyporheic zone and found that the natural attenuation of metals in the surface water of a contaminated urban river was limited by poor connectivity of the hyporheic zone, but the transport pattern of metals in hyporheic zone remains unclear. Some previous studies also provide valuable insights into factors driving the adsorption and transformation of metals, and found that metal sulfide deposits and bacteriogenic sulfides in river sediments enhance the adsorption of heavy metals, while high sediment permeability prevents accumulation of heavy metals in riverbeds [38]. The transformation of metals in the hyporheic zone is influenced by water movement, permeability, substrate particle size, resident biota, and the physiochemical features of the overlying stream and adjacent aquifers [39]. In spite of this, these previous studies concentrated more on the surface water and interface exchange in rivers, but not on the inner area of the hyporheic zone.

In order to better understand transport and fate of metal ions in the hyporheic zone, flume experiments and simulations are investigated here. We describe experiments with flow over a streambed with periodic bedforms, which induces interactions between the bed and the overlying water, i.e., the flow/bedform interaction generates hydraulic gradients that drive pore water flow in the hyporheic zone (Fig. 1a, b). Zn^{2+} ions are used as the transported metal within the overland flow [34,35], while the bedforms are triangular, similar to previous experiments [40,41,42]. Given that the transport of metal ions in the streambed is determined by pore water flow and adsorption (Fig. 1c), the main purpose of this study is to investigate 1) how does adsorption affect the transport of metal ions in the streambed? and 2) what are the transport and distribution characteristics of metals in the hyporheic zone?

2 Laboratory experiments

2.1 Flume and sand

Experiments were conducted in an indoor recirculating flume for physical modeling of a river with uniform triangular bedforms (Fig. 1a). The wall of the flume is made of transparent glass, permitting imaging of the experiments. The effective length of the sand bed is about 10 m; its height varied from 12.0 cm at the trough to 14.0 cm at the crest (Fig. 1b, Table 1); the average overlying water depth was 8.22 cm (Table 1). A transducer was installed at the tail end of the flume for monitoring the temperature, conductivity, pH and salinity of the overlying water.

The bedform was made of silica sand from the Yangtze River, which was sieved to 0.25 - 0.60 mm with a median grain size of $d = 0.387$ mm. The bulk porosity (θ) was measured as 0.33 with the water evaporation method. The saturated hydraulic conductivity was $K = 8.84 \times 10^{-4}$ m s^{-1}, determined using the constant-head method. Both properties were assumed to remain constant during the experiments [43]. Before the experiments, the sand was washed to remove metal ions, oxides, organic matter and other impurities [44]. The sand washing steps were: 1) Washing with deionized water four times, 45 mins each time; 2) washing with an acidic solution at pH 3.5 for 8-9 h; 3) repeat the washing in step 1 three more times; 4) repeat step 2 with a solution at pH 10.5; 5) repeat step 1 three times. In the experiments, the pH of the flume effluent was 6.8.

2.2 Experiments and measurements of Zn^{2+} concentrations

The washed sand was packed into the flume, then the bedform stability was checked by overland flow. Subsequently, NaCl was added to the overlying water to give an initial ionic strength of 7.5 mM based on previous work [44]. Buffer ($NaHCO_3$ solution) was added to maintain the pH around 7 in the flume surface water. Finally, $ZnCl_2$ solution was uniformly added to the flow. The experiment lasted for about 3 d, during which 400 ml of deionized water was added every 4 h to replace evaporated water. The pH was monitored periodically and maintained using buffer solutions. During the initial 30 min, the overlying water was simultaneously extracted from three different positions (entry, midpoint, exit) of the flume. After 30 min, it was extracted only at the exit of the flume because the solute was almost uniform in the overlying water [44]. In addition, 0.25 mL of pore water was extracted from sampling points (Fig. 1b) using Hamilton (Switzerland) micro-samplers (outer diameter: 0.72 mm; inner diameter: 0.15 mm; length: 51 mm). Then, samples were placed in a 4-mL glass bottle and diluted with 2 mL of deionized water. The NaCl samples were measured in situ using electrical conductivity (EC) assuming a linear relationship between concentration and EC [42]. For zinc, sample vials were sealed and refrigerated for subsequent measurement using ICP-MS.

3. Numerical simulations, adsorption models and coefficients

Stream water flow, pore water flow, and reactive and nonreactive solute transport in the streambed were simulated based on one-way sequential couplin [41,45-47]. Stream water flow was computed using the 2D CFD package, FLUENT, based on the Reynolds-Averaged Navier-Stokes equations together with the k-ω turbulence closure scheme [44]. The predicted pressures at the bed surface were used as boundary conditions in a 2D COMSOL-based model for simulation of pore water flow and reactive and nonreactive solute transport in the streambed. The pore water flow was modeled using Darcy's Law and the continuity equation for incompressible flow in a non-deformable medium based on boundary conditions described by *Jin et al.* [44]. Finally, the transport of reactive and nonreactive solutes was simulated based on the pore water flow field. The mesh selection is discussed in Section S1 (S refers to Supplementary Material).

3.1 Pore water flow

COMSOL Multiphysics was used to model the flow and solute transport in the bed. The pore water flow is governed by the combination of Darcy's Law and the continuity equation for incompressible flow in a non-deformable medium, and thus the groundwater flow can be described as (constant fluid density assumed):

$$\frac{\partial u_i}{\partial x_i} = 0 \tag{1}$$

$$u_i = -\frac{K}{\theta}\frac{\partial h}{\partial x_i} \tag{2}$$

where θ (-) is the volumetric porosity, K (m s^{-1}) is the hydraulic conductivity, u_i (i = 1, 2) is the pore water flow velocity component in the x_i (i = 1, 2) direction and h is the hydraulic head. Simulation parameters are shown in Table 1 and boundary condition are shown in Fig. S2a.

3.2 Mass transport

The linear adsorption equilibrium adsorption [48], were considered in the simulation. The linear isothermal adsorption equation is described as [34],

$$S = K_{ad}C \tag{3}$$

where S (kg kg^{-1}) is the adsorbed mass per bulk mass, C (kg m^{-3}) is the equilibrium concentration of contaminants in the pore water, K_{ad} (m^3 kg^{-1}) is the equilibrium constant for linear adsorption. The linear adsorption model satisfactorily describes this experiment (Section 4).

Using Eq. 3, the zinc ion transport is given by:

$$(1+\frac{\rho_b}{\theta}K_{ad})\frac{\partial C}{\partial t} = \frac{\partial}{\partial x_i}\left(D_{ij}\frac{\partial C}{\partial x_j} - u_i C\right) \tag{4}$$

where ρ_b (kg m^{-3}) is the bulk density and D_{ij} (m^2 s^{-1}) is the 2D dispersion coefficient tensor:

$$D_{ij} = (\alpha_T |u| + D_e)\delta_{ij} + (\alpha_L - \alpha_T) u_i u_j / |u| \tag{5}$$

Here, α_L and α_T are the longitudinal and transverse dispersivities, respectively; $|u| = \sqrt{u_1^2 + u_2^2}$ is the magnitude of the pore water flow velocity; and D_e is the effective molecular diffusion coefficient.

3.3 Boundary conditions for mass transport

The boundary conditions for metal ion transport were set as follows (Fig. S2): (1) periodic conditions with $C(0, x_2, t) = C(L, x_2, t)$ and $\partial C(0, x_2, t)/\partial x_2 = \partial C(L, x_2, t)/\partial x_2$ were imposed on the lateral boundaries ($x_1 = 0, L$) of the domain. Note that only one bedform was simulated as the processes and conditions for different bedforms were assumed to behave similarly; (2) a no-flux condition was imposed on the bottom boundary of the domain, giving a zero concentration gradient $\partial C / \partial x_2 \big|_{x_2=0} = 0$ [49,50]; and (3) the following boundary conditions were imposed along the sediment-water interface:

$$\begin{cases} C = C_t & \mathbf{n} \bullet \mathbf{u} \geq 0 \\ \dfrac{\partial C}{\partial \mathbf{n}} = 0 & \mathbf{n} \bullet \mathbf{u} < 0 \end{cases} \tag{6}$$

where **n** is the unit vector normal to the interface (pointing inward), **u** is the flow velocity vector of metal ions, and C_t (kg m^{-3}) is the concentration of metal ions in the overlying water at time *t*. The overlying water in our experiments was well mixed and hence a spatially uniform concentration was assumed along the flume. However, C_t varies with time due to mass exchange between the overlying water and the bed:

$$C_t = \frac{C_0 V_o - B \iint \left(\theta C(x_1, x_2, t) + \rho_b S(x_1, x_2, t) \right) dA}{V_o}, \tag{7}$$

where V_o (m^3) is the total water volume in the flume system excluding V_p (pore water in the streambed), $C(x_1,x_2,t)$ and $S(x_1,x_2,t)$ are, respectively, the simulated concentrations of metal ions in the pore water and adsorbed metal ions in the sand at location (x_1,x_2) and time t, B (m) is the width of the flume, and A (m^2) is the area (on the x_1-x_2 plane shown in Fig. S2) of the bed in the flume. The integral in Eq. 7 gives the mass of ions retained in the bed.

3.4 Calibration of equilibrium constant (*K_{ad}*)

Batch adsorption experiments were conducted to obtain the equilibrium constant for linear adsorption (K_{ad}). First, 150 g of dried sand was added to 150 mL of 7.5 mM NaCl solution, then Zn^{2+} (at various initial concentrations in the range 0.010-0.040 mM) was added keeping the pH (range 2-9) fixed ($NaHCO_3$ buffer). The resulting mixtures were shaken for 48 h in order to reach equilibrium. The adsorption time of Zn^{2+} ions was determined before the batch adsorption experiments (Fig. 2a).

Exchange of Zn^{2+} with the soil is assumed to follow the reaction [34]:

$$\mathrm{SiOH{+}Zn^{2+}} \leftrightarrow \mathrm{SiOZn^{+}{+}H^{+}} \tag{8}$$

where SiOH is the surface hydroxyl species of silica sand, and $SiOHZn^+$ are adsorbed phase Zn^{2+} ions. The equilibrium constant (K_{Zn}) of this reaction is [51]:

$$K_{Zn} = \frac{[\mathrm{SiOZn^+}][\mathrm{H^+}]}{[\mathrm{SiOH}][\mathrm{Zn^{2+}}]}\exp\left|\frac{F\psi_0}{R_0T}\right| \tag{9}$$

where F (96493.5 J V^{-1} eq^{-1}) is the Faraday constant, Ψ_0 (V) is the potential on the surface of silica sand, R_0 (8.3147 J mol^{-1} K^{-1}) is the gas constant, T (°K) is the temperature and the brackets indicate activity. As [SiOH] = 1, Eq. 9 can be converted into (base 10 logarithm):

$$\log(K_{Zn}) - \log(\exp\left|\frac{F\psi_0}{R_0T}\right|) + \mathrm{pH} = \log[\mathrm{SiOZn^+}] - \log[\mathrm{Zn^{2+}}] \tag{10}$$

Later, we use $\varphi = \log(K_{Zn}) - \log(\exp\left|\frac{F\psi_0}{R_0T}\right|)$ in this expression.

The adsorbed proportion (P_{ST}) is defined as the ratio of adsorbed mass to the total mass (assuming activities can be replaced by concentrations):

$$P_{ST} = \frac{[\mathrm{SiOZn^+}]}{[\mathrm{SiOZn^+}] + [\mathrm{Zn^{2+}}]} \tag{11}$$

Using Eq. 10 and approximating activities by molarity reduces Eq. 11 to:

$$P_{ST} = \left(1 + 10^{-\varphi - \mathrm{pH}}\right)^{-1} \tag{12}$$

The fits of this equation to the measured adsorption data are found in Fig. 2b, which involve fitting φ. For the conditions of the flume experiment (φ = -6.003, C_{M0} = 0.036 mM, pH = 6.8), the adsorbed proportion P_{ST} = 0.8622. The equilibrium constant for linear adsorption is then found using:

$$K_{ad} = \frac{\theta}{\rho_b}\frac{P_{ST}}{1 - P_{ST}} \tag{13}$$

4. Results and Discussion

The concentrations of NaCl and Zn^{2+} in both overlying water and pore water were measured and simulated with the transport model described above. The effects of the dispersion coefficient (α) and equilibrium constant (K_{ad}) on the transport of metal ions are then examined.

4.1 NaCl and Zn^{2+} concentrations in the overlying water

The NaCl concentration in the overlying water decreased rapidly during the first 5 h of the experiment (Fig. 3), which can be attributed to the rapid migration of NaCl from the overlying water to the shallow area of the bedform with a large pore water velocity and associated solute migration flux. However, as the solute front passed through the shallow area, the NaCl concentration in the overlying water decreased more slowly. Finally, the value of C/C_0 for NaCl reached a stable level at around 0.75. Given that there is no adsorption or reaction of NaCl, NaCl would be uniformly distributed in the whole system after an infinite time, i.e., $V_o/(V_o + V_p) = 0.75$. A more dramatic decrease is noted for the Zn^{2+} concentration in the overlying water as it is driven by both advection and adsorption. For Zn^{2+}, the normalized concentration (C/C_0) reaches a stable level lower than 0.40 (Fig. 3), which is much lower than that of NaCl due to the adsorption of Zn^{2+} by the streambed.

4.2 Variation of Zn^{2+} concentration in the bedform

The measured and modeled Zn^{2+} concentrations in the monitoring profiles N1 and N2 (Fig. 1b) at different times are shown in Fig. 4. The modeled results generally compare well with the measurements. Two characteristic coefficients are introduced to describe the intrusion of NaCl and Zn^{2+}, the maximum-initial concentration ratio ($R_m = C_m/C_0$) and intrusion depth (D_{in}), where C_m is the maximum concentration in a monitoring column at a specific time, and D_{in} is the depth at which the concentration is $C_m/2$ (Fig. S3).

The simulated D_{in} of Zn^{2+} is much shallower compared with measured D_{in} at 25 min and from 123 - 1825 min the measured and modeled D_{in} are almost at same level regardless of errors (Fig. 4a), possibly because of the assumption of equilibrium adsorption of Zn^{2+} used in the model (Fig. 2a suggests the characteristic time of the adsorption kinetics to be 10-20 mins). Both the measurements and simulations show that the Zn^{2+} profiles have lower concentrations near the surface boundary than the maximum concentration measured in the streambed. This occurs due to the continuous reduction of the Zn^{2+} concentration in the overlying water [52]. The simulations of zinc concentrations in the streambed reflect this change, i.e., the initial high concentration in the stream result in higher concentrations deeper in the streambed, and lower concentrations near the stream-streambed boundary. The same behavior occurs in the NaCl case, although the reduction in the concentration near the top of the streambed is not obvious. For the concentration distribution in the whole bedform, the intrusion area increases and the maximum concentration decreases (Fig. S4) over time. For the linear adsorption isotherm, the distributions of C/C_0 and S/S_0 are the same (Fig. S5).

The R_m values show a rapidly increasing trend at the beginning of experiment and then slowly decrease, while the magnitude of D_{in} increases with time for both NaCl and Zn^{2+} (Fig. 5). When comparing the differences between NaCl and Zn^{2+}, the R_m values for NaCl are larger than those of Zn^{2+}. As well, the corresponding D_{in} values are also greater, as expected, due to adsorption of Zn^{2+} (Figs. 4, 5). When comparing the differences between profiles N1 and N2, the curves for both D_{in} and R_m are obviously delayed (Fig. 5). A sharp decreasing trend is observed at the end of the NaCl curves in Fig. 5b, because the solute has reached the bottom of the profile but the intrusion depth (D_{in}) has not reached the bottom (Figs. S3c).

4.3 Variation of Zn^{2+} mass in three phases

Fig. 6 illustrates the trends of Zn^{2+} mass in three phases: overlying water, pore water and adsorbed to the streambed. Fig. 6a shows the modeled predictions for each phase, as well as Zn^{2+} in the overlying water from measurements (assumed to be well mixed [42]). The mass of Zn^{2+} ions decreases in the overlying water but increases in pore water as the adsorption is assumed to be instantaneous (Fig. 6a). The mass of Zn^{2+} in the overlying water decreases rapidly in the first few hours of the experiment, then reduces more slowly. Correspondingly, the mass of Zn^{2+} in the pore water and adsorbed phase show opposite trends. Because of instantaneous sorption, the adsorbed mass of Zn^{2+} is 6.26 times of the mass in pore water (Fig. 6b), as computed from:

$$P_{SC} = \frac{mass\ adsorbed\ to\ soil}{mass\ in\ pore\ water} = \frac{\int_{m} S\, dm}{\int_{V_p} C\, dV_p} = \frac{\rho_b K_{ad}}{\theta} \tag{14}$$

where *m* (kg) is the mass of sand. As the equilibrium constant (K_{ad}) is fixed for constant pH (Eq. 13), P_{SC} is also constant. As seen above (Eqs. 3, 4), the partitioning of Zn depends on K_{ad} and hence pH. For fixed pH, the adsorbed mass of Zn increases with K_{ad} and the total mass in overlying water and pore water become smaller (Fig. 6c). Correspondingly, as K_{ad} reduces, so does the total adsorbed mass so that in the limit of no sorption ($K_{ad} = 0$), we recover the case of NaCl (Fig. 6c). The mass ratio of the overlying water phase to pore water phase (P_{OC}) is defined as:

$$P_{OC} = \frac{mass\ in\ overlying\ water}{mass\ in\ pore\ water} = \frac{\int_{V_o} C_t\ \ dV_o}{\int_{V_p} C\, dV_p} \tag{15}$$

Similarly, we define the mass ratio of the adsorbed mass to the mass in the overlying water phase (P_{SO}) is defined as:

$$P_{SO} = \frac{mass\ adsorbed\ to\ soil}{mass\ in\ overlying\ water} = \frac{\int_{m} S\, dm}{\int_{V_o} C_t\ \ dV_o} \tag{16}$$

i.e., $P_{SC} = P_{SO}P_{OC}$.

Even though P_{SC} is constant for all *t*, both P_{SO} and P_{OC} vary with *t* (Fig. 6b). Assuming that no zinc is lost from the experiment, in the long-time limit it will be distributed with uniform concentrations in each of the water and soil phases, i.e., the concentrations in the overlying and pore water will be identical, and the adsorbed concentrations will be uniform throughout the streambed. To generalize the results slightly, we assume that the volume of overlying water is *M* times that of the pore water (in our experiment, $M = 3$). Then, it is straightforward to show that, for large *t* :

$$P_{SO} = \frac{\rho_b K_{ad}}{M\theta} \quad (17)$$

$$P_{OC} = M \quad (18)$$

Under the given assumptions, the time scale beyond which Eqs. 17 and 18 hold is defined by the time needed for zinc to spread throughout the porous medium, i.e., it is defined by the flow conditions, and not the reaction kinetics of zinc adsorption.

4.4 The effects of dispersivities (*α*)

Fig. 7 (and Fig. S6) illustrates the effects of dispersivities (α) on the concentration in the overlying water, and the Zn distribution in the bedform. Thus, the variation of α does not affect the concentration in the overlying water (Fig. 7a) as well as the exchange rate between the stream and streambed. However, in terms of the concentration distribution in the bedform, a larger α results in a wider concentration transition zone (Figs. 7b, S6). In spite of this, the concentration distribution above the transition zone is almost the same for different values of α (Fig. 7b). The maximum-initial concentration ratio ($R_m = C_m/C_0$) is also affected by α (Fig. 7c). The smaller α is, the larger R_m would be, i.e., the diffusive flux is less and the maximum concentrations are increased. The variation of α hardly affects the intrusion depth (D_{in}), i.e., D_{in} is controlled by advection rather than dispersion (Fig. 7c).

4.5 Effects of equilibrium constants (*K_{ad}*)

Here, we consider the effects of different K_{ad} values (i.e., for different pH values, held constant in a given experiment). For this, two characteristic parameters are defined: the final stable concentration (C_f) and the time to reach half of this concentration (T_h). Note that $C_f = C(x_1,x_2,t \rightarrow \infty)$. Using the same assumptions as in Section 4.3, we find that:

$$m_{Zn,\,total} = C_f V_p \left(M + 1 + \frac{\rho_b K_{ad}}{\theta} \right) \tag{19}$$

where $m_{Zn,total}$ is the total mass of zinc in the system (adsorbed and in the water phase). For fixed $m_{Zn,total}$, it is clear from Eq. 19 that C_f decreases as K_{ad} increases, as can be seen in Fig. 8 (and Fig. S6). However, the range of T_h/T_{h0} (0.7 to 1.1) is relatively small compared with the range of K_{ad}/K_{ad0} (ranging from 0 to 4.0). When K_{ad}/K_{ad0} increases from 0 to 0.5, the T_h/T_{h0} increases from 0.7 to 1.1, i.e., the time scale to reach a stable concentration is noticeable. On the contrary, when K_{ad}/K_{ad0} increases from 0.5 to 4, the T_h/T_{h0} gradually drops from 1.1 to 0.8. These results show that the time to reach steady state is, as already noted above, is mainly due to the flow conditions than to the value of the equilibrium constant, K_{ad}.

The intrusion depth (D_{in}) and the maximum-initial concentration ratio ($R_m = C_m/C_0$) decrease with K_{ad} (Fig. 9), because more Zn^{2+} ions would be adsorbed and thus less Zn^{2+} ions would be retained in pore water. Figure 9 shows that R_m at profiles N1 and N2 is nearly identical, i.e., insensitive to K_{ad}. However, the range of D_{in} is greater for profile N2 compared to N1, i.e., D_{in} varies in a wider range on the lee-side of bedform as K_{ad} varies.

The intrusion depth (D_{in}) becomes deeper and the maximum-initial concentration ratio (R_m) becomes smaller over time (Fig. S9) even for NaCl (Fig. S3c). Fig. S9 shows that adsorption can significantly reduce the intrusion depth (D_{in}) and the maximum-initial concentration ratio (R_m). And the maximum-initial concentration ratio (R_m) reduces also with larger K_{ad} (Fig. S9), indicating that the concentration of contaminants in the overlying water also decreases over time (Fig. S7). Thus, the decrease in the maximum-initial concentration ratio (R_m) of Zn^{2+} over time (Fig. S9) can be attributed to the decreasing concentration in the overlying water and adsorption in the bedform. A comparison of Fig. S4a and b shows that the intrusion depth (D_{in}) is deeper on the stoss side of the bedform, but the maximum-initial concentration ratio (R_m) remains almost unchanged on both sides, indicating that the intrusion time on the lee side is postponed.

The maximum-initial concentration ratio (R_m) increases sharply and then decreases slowly to a stable level; whereas the intrusion depth (D_{in}) increases continuously (Fig. S10). Comparisons of Fig. S10a & b and Fig. 9c & d show that the time is postponed in Fig. S10b & d because ions are first migrated to the stoss side (N1) and then slowly carried out from the lee side (N2). A sharp decreasing trend is observed at the end of case $K_{ad} = 0.25K_{ad0}$ in Fig. S10c, because the front tip of the concentration intrusion curve has reached the bottom of the profile ahead of the intrusion depth (D_{in}) (Fig. S3). As the intrusion depth (D_{in}) reaches the bottom of the bedform, it is maintained at -12 cm (Fig. S10c, Fig. S3c), as is apparent for NaCl in Fig. S10c.

A new coefficient, the half depth arrival time (T_a) at which the intrusion depth D_{in} = -6 cm (Fig. S10), is defined to represent the time for the intrusion line to reach a certain depth. Fig. 10 shows that there is a linear correlation between the half depth arrival time (T_a) and the equilibrium constant for linear adsorption (K_{ad}), and thus the larger the value of K_{ad}, the longer the arrival time will be. However, it is noted that the arrival times are delayed on the lee side of the bedform.

All these results suggest that adsorption prevents the intrusion of ions into the streambed, which can reduce the pollution of groundwater but can also cause higher accumulation of contaminated metals in the hyporheic zone, and as a consequence secondary pollution may occur if these metal ions are released back to the overlying water.

6. Conclusions

In this study, experiments and numerical simulations were performed to investigate the adsorption of Zn^{2+} ions and their transport in the hyporheic zone. The main conclusions are:

1) Adsorption leads to a more rapid decrease of Zn^{2+} concentration in the overlying water compared with non-adsorbing case (NaCl). The variation of Zn^{2+} concentration in the overlying water is sensitive to the equilibrium constant. The larger the adsorption coefficient is, the more rapidly the concentration decreases.

2) The mass in three phases varies rapidly at beginning (increasing in pore water and adsorbed phase, decreasing in overlying water) and finally reaches an equilibrium. The sum of Zn^{2+} in pore water and adsorbed phase is strictly equal to the decreasing mass in overlying water. The adsorbed mass of metal ions is more than 6 times higher than the pore water phased mass.

3) The strong function of adsorption prevents the intrusion of ions into the streambed and thus mitigates the pollution of groundwater, but will also cause higher accumulation of contaminated metals in the shallower layer of hyporheic zone.

Knowledge of the transport of metal ions in the hyporheic zone may provide important insights into the restoration of polluted rivers. Next important research direction is to elucidate the interactions of metal ions and particles in the hyporheic zone. Fine sediments and colloidal particles can act as a carrier of metal ions [34, 43], which may lead to higher accumulations of contaminants in the hyporheic zone.

Acknowledgments

This research has been supported by the Natural Science Foundation of China (51679065), the Basic Research Programs (Natural Science Foundation) of Jiangsu Province (BK20171436), Social Development - Major Demonstration of Science and Technology of Science and Technology Projects of Jiangsu Province (BE2018737); and the 111 Project (B17015), Ministry of Education and State Administration of Foreign Experts Affairs, P. R. China.

References

1 Järup, L. (2003). Hazards of heavy metal contamination. British medical bulletin, 68(1), 167-182. https://doi.org/10.1093/bmb/ldg032

2 Islam, M. S., Ahmed, M. K., Raknuzzaman, M., Habibullah-Al-Mamun, M., & Islam, M. K. (2015). Heavy metal pollution in surface water and sediment: A preliminary assessment of an urban river in a developing country. Ecological Indicators, 48, 282-291.https://doi.org/10.1016/j.ecolind.2014.08.016

3 Varol, M. (2011). Assessment of heavy metal contamination in sediments of the Tigris River (Turkey) using pollution indices and multivariate statistical techniques. Journal of Hazardous Materials, 195, 355-364.https://doi.org/10.1016/j.jhazmat.2011.08.051

4 Liu, G., Tao, L., Liu, X., Hou, J., Wang, A., & Li, R. (2013). Heavy metal speciation and pollution of agricultural soils along Jishui River in non-ferrous metal mine area in Jiangxi Province, China. Journal of Geochemical Exploration, 132, 156-163.https://doi.org/10.1016/j.gexplo.2013.06.017

5 Milenkovic, N., Damjanovic, M., & Ristic, M. (2005). Study of Heavy Metal Pollution in Sediments from the Iron Gate (Danube River), Serbia and Montenegro. Polish Journal of Environmental Studies, 14(6).

6 Jabłońska-Czapla, M., Nocoń, K., Szopa, S., & Łyko, A. (2016). Impact of the Pb and Zn ore mining industry on the pollution of the Biała Przemsza River, Poland. Environmental monitoring and assessment, 188(5), 262.https://doi.org/10.1007/s10661-016-5233-3

7 Li, X., Wai, O. W., Li, Y. S., Coles, B. J., Ramsey, M. H., & Thornton, I. (2000). Heavy metal distribution in sediment profiles of the Pearl River estuary, South China. Applied Geochemistry, 15(5), 567-581.https://doi.org/10.1016/s0883-2927(99)00072-4

8 Haileslassie, T., & Gebremedhin, K. (2015). Hazards of heavy metal contamination in ground water. International Journal of Technology Enhancements and Emerging Engineering Research, 3(2), 1-6.

9 Giller, K. E., Witter, E., & McGrath, S. P. (1998). Toxicity of heavy metals to microorganisms and microbial processes in agricultural soils: A review. Soil biology and biochemistry, 30(10-11), 1389-1414.https://doi.org/10.1016/s0038-0717(97)00270-8

10 Ogunleye, P. O., Mayaki, M. C., & Amapu, I. Y. (2002). Radioactivity and heavy metal composition of Nigerian phosphate rocks: Possible environmental implications. Journal of environmental radioactivity, 62(1), 39-48.https://doi.org/10.1016/s0265-931x(01)00149-7

11 Dalmacija, B., Prica, M., Ivancev-Tumbas, I., Van der Kooij, A., Roncevic, S., Krcmar, D., ... & Teodorovic, I. (2006). Pollution of the Begej Canal sediment-metals, radioactivity and toxicity assessment. Environment International, 32(5), 606-615.https://doi.org/10.1016/j.envint.2006.01.006

12 Bajracharya, K., Y. T. Tran, and D. A. Barry. 1996. Cadmium adsorption at different pore water velocities. Geoderma. 73(3-4): 197-216. DOI: 10.1016/0016-7061(96)00048-1

13 Gandy, C. J., Smith, J. W. N., & Jarvis, A. P. (2007). Attenuation of mining-derived pollutants in the hyporheic zone: A review. Science of the Total Environment, 373(2-3), 435-446. https://doi.org/10.1016/j.scitotenv.2006.11.004

14 Borgmann, U., & Norwood, W. P. (1997). Toxicity and accumulation of zinc and copper in Hyalella azteca exposed to metal-spiked sediments. Canadian Journal of Fisheries and Aquatic Sciences, 54(5), 1046-1054.https://doi.org/10.1139/f97-020

15 Kookana, R. S., R. Naidu, D. A. Barry, Y. T. Tran, and K. Bajracharya. 1999. Sorption-desorption equilibria and dynamics of cadmium during transport in soil. In Fate and Transport of Heavy Metals in the Vadose Zone. Editors: H. M. Selim and I. K. Iskandar, Lewis Publishers, Boca Raton, Florida, Chapter 3, pp. 59-90.

16 Al Bakheet, S. A., Attafi, I. M., Maayah, Z. H., Abd-Allah, A. R., Asiri, Y. A., & Korashy, H. M. (2013). Effect of long-term human exposure to environmental heavy metals on the expression of detoxification and DNA repair genes. Environmental Pollution, 181, 226-232.https://doi.org/10.1016/j.envpol.2013.06.014

17 Ou, X., Zhang, Y., Xu, C., Lin, X., Zang, Q., Zhuang, T., ... & Liu, B. (2012). Transgenerational inheritance of modified DNA methylation patterns and enhanced tolerance induced by heavy metal stress in rice (Oryza sativa L.). PloS One, 7(9), e41143.https://doi.org/10.1371/journal.pone.0041143

18 Dallinger, R., Prosi, F., Segner, H., & Back, H. (1987). Contaminated food and uptake of heavy metals by fish: A review and a proposal for further research. Oecologia, 73(1), 91-98.https://doi.org/10.1007/bf00376982

19 Cheng, Z., Man, Y. B., Nie, X. P., & Wong, M. H. (2013). Trophic relationships and health risk assessments of trace metals in the aquaculture pond ecosystem of Pearl River Delta, China. Chemosphere, 90(7), 2142-2148.https://doi.org/10.1016/j.chemosphere.2012.11.017

20 Türkdoğan, M. K., Kilicel, F., Kara, K., Tuncer, I., & Uygan, I. (2003). Heavy metals in soil, vegetables and fruits in the endemic upper gastrointestinal cancer region of Turkey. Environmental toxicology and pharmacology, 13(3), 175-179.https://doi.org/10.1016/s1382-6689(02)00156-4

21 Triska, F. J., Kennedy, V. C., Avanzino, R. J., Zellweger, G. W., & Bencala, K. E. (1989). Retention and transport of nutrients in a third ‐ order stream in northwestern California: Hyporheic processes. Ecology, 70(6), 1893-1905. DOI: 10.2307/1938120

22 Triska, F. J., Kennedy, V. C., Avanzino, R. J., Zellweger, G. W., & Bencala, K. E. (1989). Retention and transport of nutrients in a third ‐ order stream: Channel processes. Ecology, 70(6), 1877-1892. DOI: 10.2307/1938119

23 Findlay S. Importance of surface-subsurface exchange in stream ecosystems: The hyporheic zone. Limnology and Oceanography, 1995, 40(1):159-164. DOI: 10.4319/lo.1995.40.1.0159

24 Boulton, A.J.; Findlay, S.; Marmonier, P.; Stanley, E.H.; Valet, H.M. (1998). The functional significance of the hyporheic zone in streams and rivers. Annual Review of Ecological Systems, 29, 59-81.https://doi.org/10.1146/annurev.ecolsys.29.1.59

25 Stubbington R. (2012). The hyporheic zone as an invertebrate refuge: A review of variability in space, time, taxa and behaviour. Marine and Freshwater Research, 63(4): 293-311. DOI: 10.1071/MF11196

26 Battin TJ , Besemer K , Bengtsson MM, et al. The ecology and biogeochemistry of stream biofilms. Nature Reviews Microbiology, 2016, 14(4):251-263. DOI: 10.1038/nrmicro.2016.15

27 Bourg, A.C.M.; Bertine, C. (1993). Biogeochemical processes during the infiltration of river water into an alluvial aquifer. Environmental Science and Technology, 27, 661-666.https://doi.org/10.1021/es00041a009

28 Zhu, H. W., Zhong, B. C., & Wang, D. Z. (2014). Sediment rarefaction resuspension and contaminant release under tidal currents. Journal of Hydrodynamics, 26(5), 827-834. https://doi.org/10.1016/S1001-6058(14)60091-3

29 Jin, G., Tang, H., Li, L., & Barry, D. A. (2015). Prolonged river water pollution due to variable-density flow and solute transport in the riverbed. Water Resources Research, 51(4), 1898-1915. https://doi.org/10.1002/2014WR016369

30 Fuller CC, Harvey JW. Reactive uptake of trace metals in the hyporheic zone of a mining-contaminated stream, Pinal Creek, Arizona. Environ Sci Technol 2000;34:1150 5.https://doi.org/10.1021/es990714d

31 Winde, F., & van der Walt, I. J. (2004). The significance of groundwater–stream interactions and fluctuating stream chemistry on waterborne uranium contamination of streams—a case study from a gold mining site in South Africa. Journal of Hydrology, 287(1-4), 178-196.ttps://doi.org/10.1016/j.jhydrol.2003.10.004

32 Fuller, C. C., & Bargar, J. R. (2014). Processes of zinc attenuation by biogenic manganese oxides forming in the hyporheic zone of Pinal Creek, Arizona. Environmental science & technology, 48(4), 2165-2172.https://doi.org/10.1021/es402576f

33 Peña, J., Kwon, K. D., Refson, K., Bargar, J. R., & Sposito, G. (2010). Mechanisms of nickel sorption by a bacteriogenic birnessite. Geochimica et Cosmochimica Acta, 74(11), 3076-3089.https://doi.org/10.1016/j.gca.2010.02.035

34 Ren, J., & Packman, A. I. (2004). Stream-subsurface exchange of zinc in the presence of silica and kaolinite colloids. Environmental Science & Technology, 38(24), 6571-6581.https://doi.org/10.1021/es035090x

35 Ren, J., & Packman, A. I. (2005). Coupled stream-subsurface exchange of colloidal hematite and dissolved zinc, copper, and phosphate. Environmental Science & Technology, 39(17), 6387-6394.https://doi.org/10.1021/es050168q

36 Palumbo-Roe, B., Wragg, J., & Banks, V. J. (2012). Lead mobilisation in the hyporheic zone and river bank sediments of a contaminated stream: Contribution to diffuse pollution. Journal of Soils and Sediments, 12(10), 1633-1640. https://doi.org/10.1007/s11368-012-0552-7

37 Palumbo-Roe, B., Banks, V. J., Bonsor, H. C., Hamilton, E. M., & Watts, M. J. (2017). Limitations on the

role of the hyporheic zone in chromium natural attenuation in a contaminated urban stream. Applied Geochemistry, 83, 108-120.https://doi.org/10.1016/j.apgeochem.2017.02.011

38 Yu, K., Duan, Y., Liao, P., Xie, L., Li, Q., Ning, Z., & Liu, C. (2019). Watershed-scale distributions of heavy metals in the hyporheic zones of a heavily polluted Maozhou River watershed, southern China. Chemosphere, 124773.https://doi.org/10.1016/j.chemosphere.2019.124773

39 Ward, A.S. (2016). The evolution and state of interdisciplinary hyporheic research. Wiley Interdisciplinary Reviews Water, 3, 83-103.https://doi.org/10.1002/wat2.1120

40 Packman, A. I., Brooks, N. H., & Morgan, J. J. (2000). Kaolinite exchange between a stream and streambed: Laboratory experiments and validation of a colloid transport model. Water Resources Research, 36(8), 2363-2372.https://doi.org/10.1029/2000wr900058

41 Cardenas, M. B., & Wilson, J. L. (2006). The influence of ambient groundwater discharge on exchange zones induced by current–bedform interactions. Journal of Hydrology, 331(1-2), 103-109.https://doi.org/10.1016/j.jhydrol.2006.05.012

42 Jin, G., Tang, H., Li, L., & Barry, D. A. (2011). Hyporheic flow under periodic bed forms influenced by low-density gradients. Geophysical Research Letters, 38(22). https://doi.org/10.1029/2011GL049694

43 Jin, G., Zhang, Z., Tang, H., Xiaoquan, Y., Li, L., & Barry, D. A. (2019). Colloid transport and distribution in the hyporheic zone. Hydrological Processes, 33(6), 932-944.https://doi.org/10.1002/hyp.13375

44 Jin, G., Tang, H., Gibbes, B., Li, L., & Barry, D. A. (2010). Transport of nonsorbing solutes in a streambed with periodic bedforms. Advances in Water Resources, 33(11), 1402-1416. https://doi.org/10.1016/j.advwatres.2010.09.003

45 Barry, D. A., C. T. Miller, and P. J. Culligan-Hensley. 1996. Temporal discretisation errors in non-iterative split-operator approaches to solving chemical reaction/groundwater transport models. Journal of Contaminant Hydrology. 22(1-2): 1-17. DOI: 10.1016/0169-7722(95)00062-3.

46 Barry, D. A., K. Bajracharya, and C. T. Miller. 1996. Alternative split-operator approach for solving chemical reaction/groundwater transport models. Advances in Water Resources. 19(5): 261-275. DOI: 10.1016/0309-1708(96)00002-4.

47 Barry, D. A., C. T. Miller, P. J. Culligan, and K. Bajracharya. 1997. Analysis of split operator methods for nonlinear and multispecies groundwater chemical transport models. Mathematics and Computers in Simulation. 43(3-6): 331-341. DOI: 10.1016/S0378-4754(97)00017-7.

48 Barry, D. A. 1992. Modelling contaminant transport in the subsurface: Theory and computer programs. In Modelling Chemical Transport in Soil: Natural and Applied Contaminants, H. Ghadiri and C. W. Rose (editors), Lewis Publishers, Boca Raton, Florida, pp. 105-144.

49 Barry, D. A., and G. Sposito. 1988. Application of the convection-dispersion model to solute transport in finite soil columns. Soil Science Society of America Journal. 52(1): 3-9. DOI: 10.2136/sssaj1988.03615995005200010001x.

50 Parlange, J.-Y., J. L. Starr, M. Th. van Genuchten, D. A. Barry, and J. C. Parker. 1992. Exit condition for miscible displacement experiments in finite columns. Soil Science. 153(3): 165-171. DOI: 10.1097/00010694-199203000-00001.

51 Dzombak, D.A., and Morel, F.M.M., 1990, Surface complexation modeling—Hydrous ferric oxide: New York, John Wiley, 393 p.

52 Jin, G., Yang, W., Xu, H., Zhang, Z., Yuan, S., Tang, H., Li, L. & Barry, D. A. (2020). Density effects on solute release from streambeds. Hydrological Processes, 34(5), 1144-1153. https://doi.org/10.1002/hyp.13655

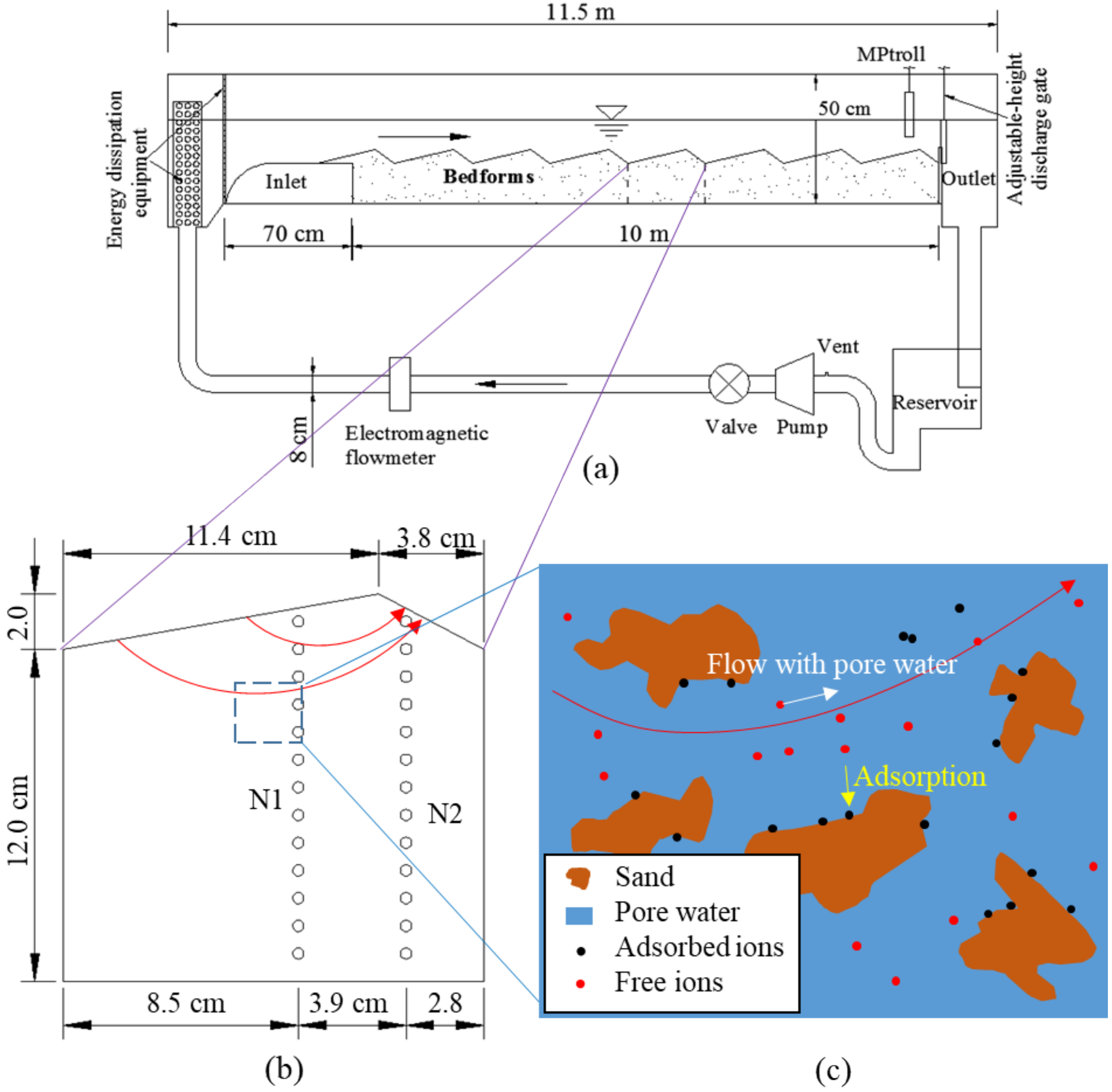

Fig. 1. (a) The circulating flume used in experiments; (b) the shape and size of a single bedform. Red arrows represent the flow direction of pore water. The open circles show sampling locations. N1 and N2 are two columns for concentration monitoring on the stoss and lee sides, respectively, of the bedform. (c) Diagrammatic sketch of the transport of ions. The red arrow represents the flow of pore water, the white arrow represents the flow of free ions with pore water, and the yellow arrows represent the sorption-desorption process.

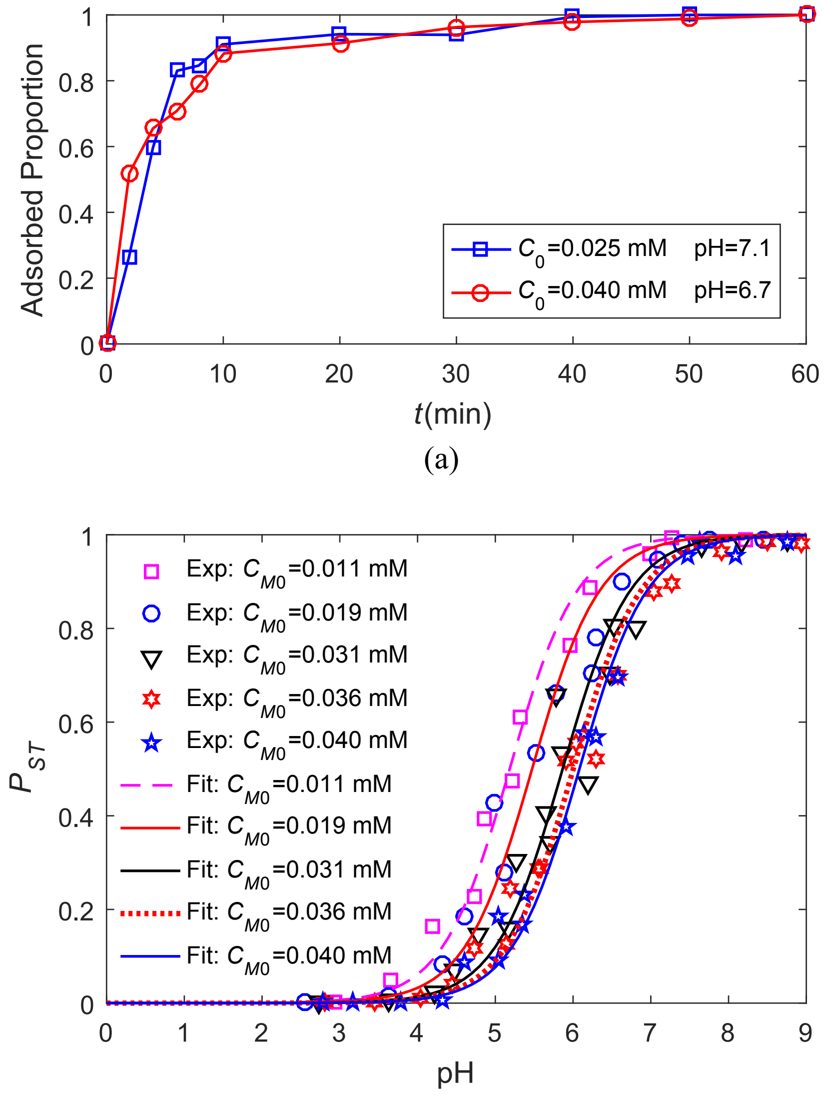

(a)

(b)

Fig. 2. (a) The adsorption kinetics between sediment and Zn^{2+}. (b) Data and fitted curves (at steady state) from batch adsorption experiments.

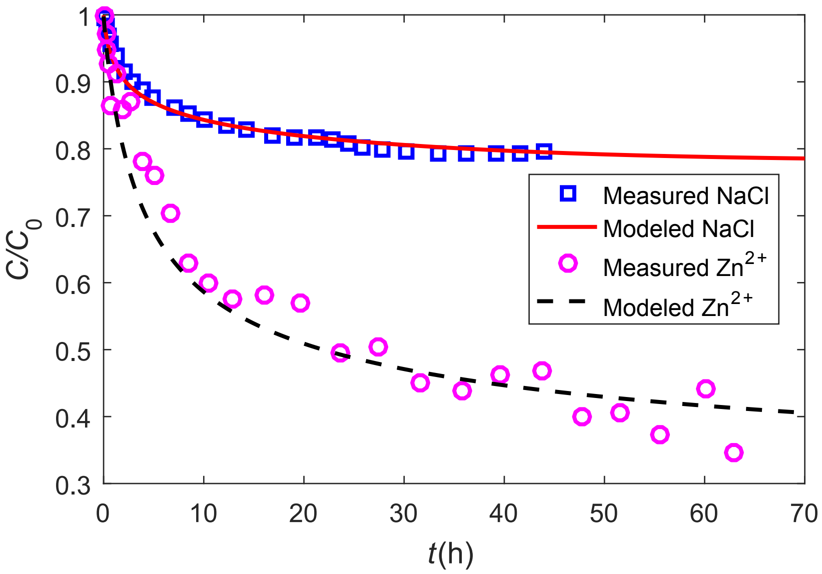

Fig. 3. Variation of Zn^{2+} and NaCl concentrations in the overlying water.

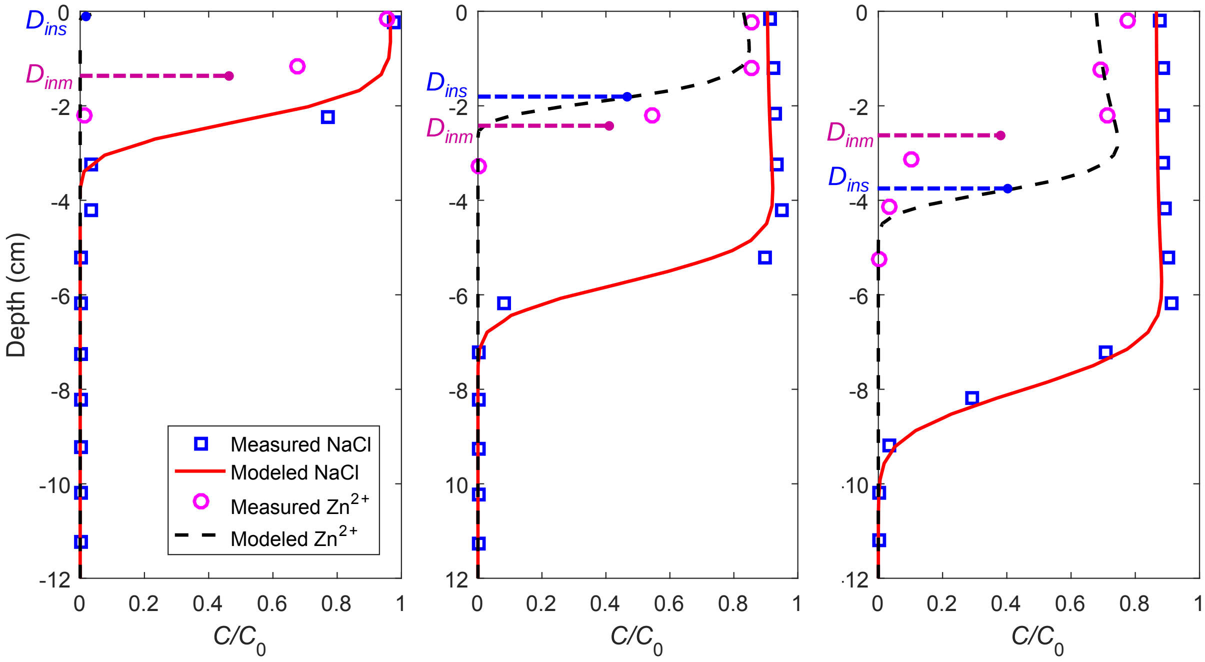

25 min 123 min 333 min

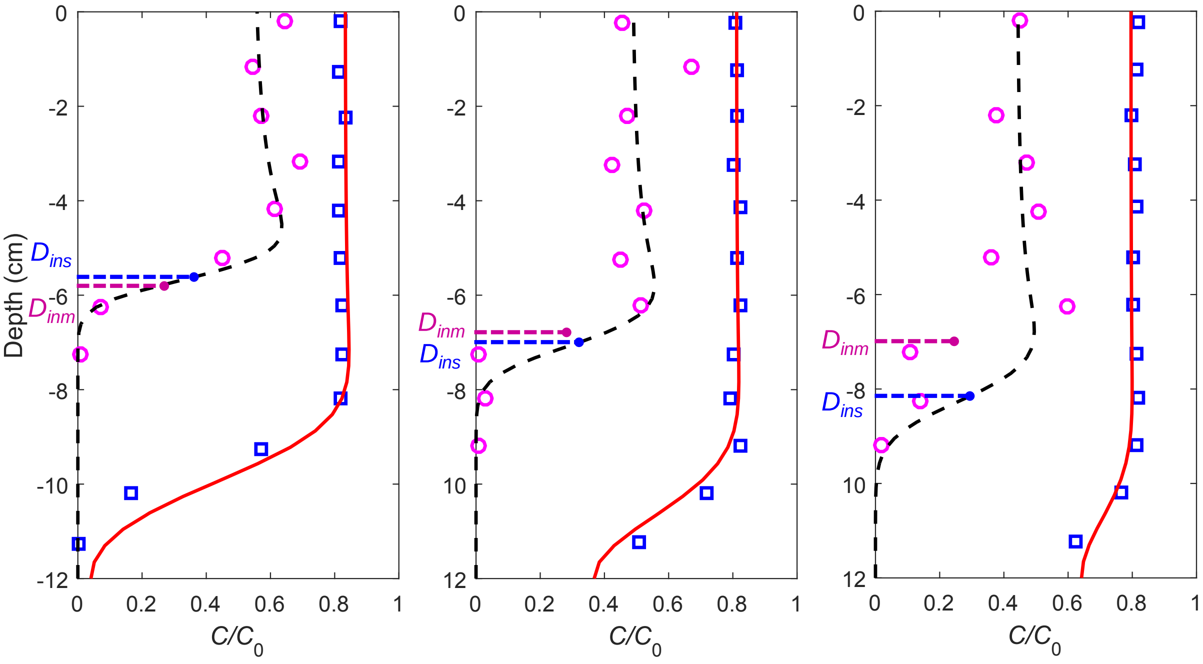

797 min 1491 min 1528 min

(a)

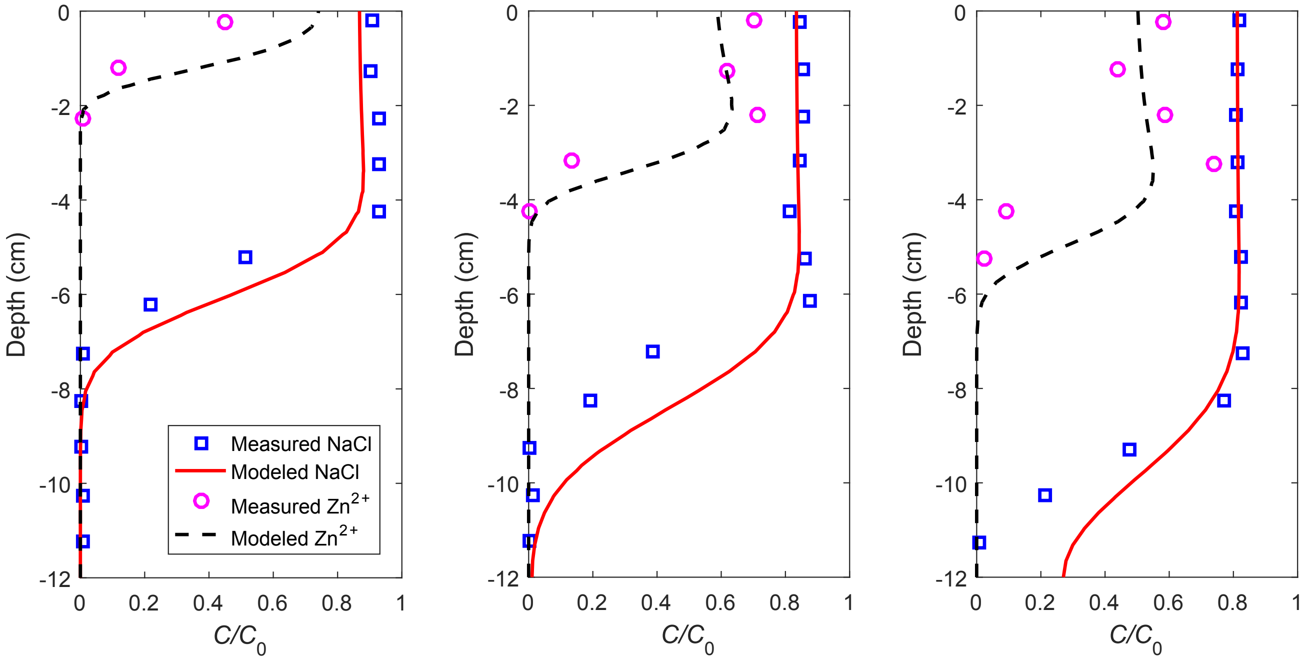

343 min

806 min

1507 min

(b)

Fig. 4. Variation of Zn^{2+} concentration in the pore water in monitoring column N1 (a) and N2 (b) at different times. The intrusion depths of Zn^{2+} from simulation (D_{ins}) and from measurement (D_{inm}) are labeled by blue and magenta dash line, respectively.

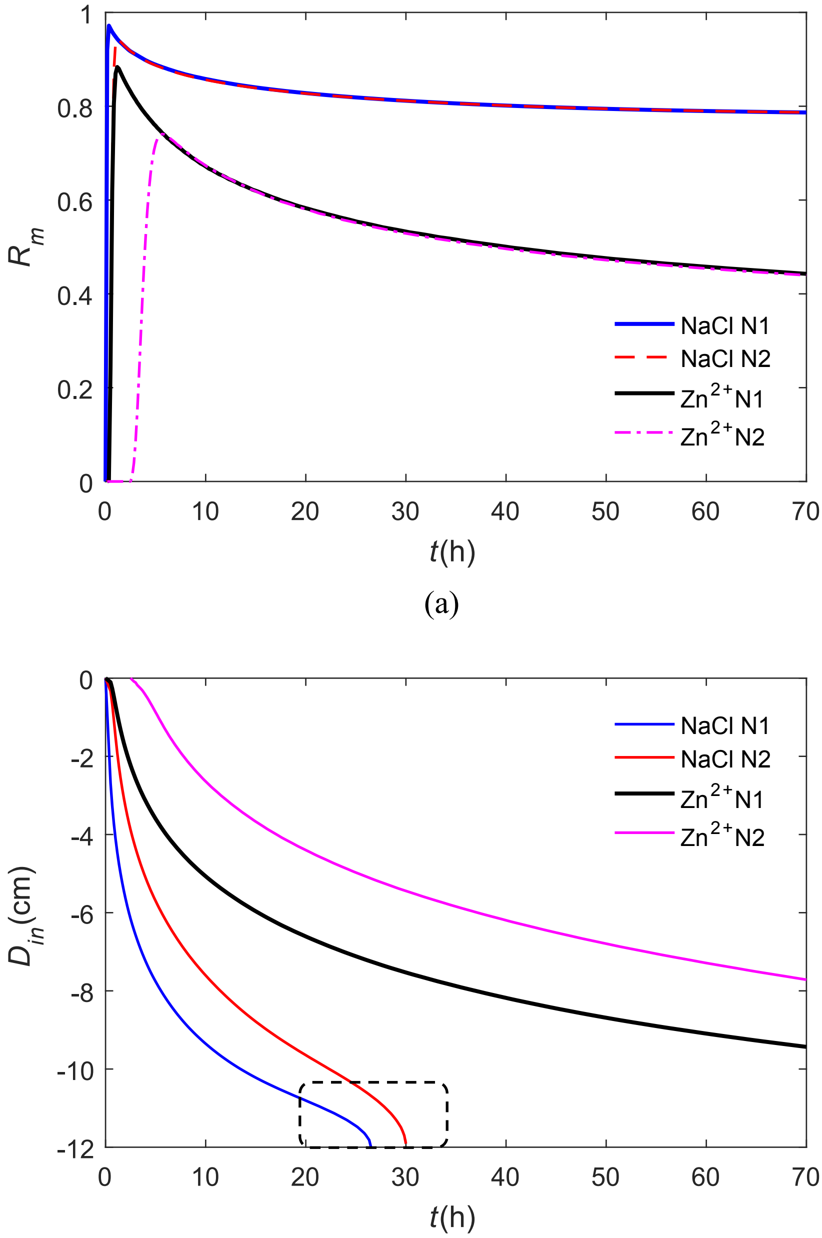

(a)

(b)

Fig. 5. The maximum-initial concentration ratio R_m (a) and intrusion depth D_{in} (b) variations for NaCl and Zn^{2+} at profiles N1 and N2. A sharp decreasing trend is observed (in the dash box) at the end of case NaCl for D_{in} because the front tip of the concentration intrusion curve has reached the bottom of the profile ahead of the intrusion depth (Fig. S6).

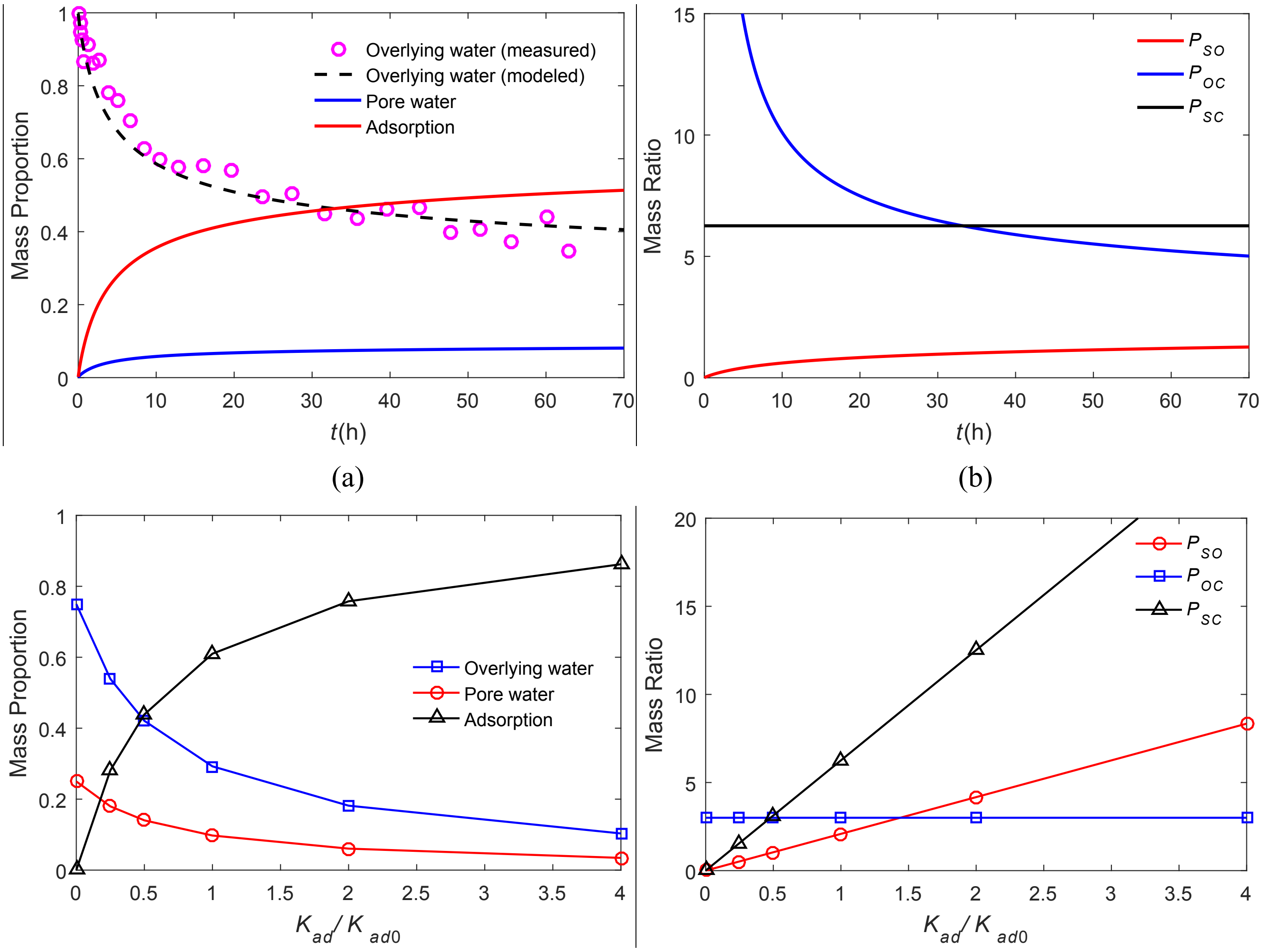

(a) (b)

(c) (d)

Fig. 6. (a) Variations of mass proportions of Zn^{2+} in three phases with time ($K_{ad} = K_{ad0}$). (b) Mass ratio of adsorption to overlying water phase (P_{SO}), overlying water phase to pore water phase (P_{OC}), and adsorption to pore water phase (P_{SC}). (c) Final stable mass proportions with different K_{ad} values. The value of K_{ad0} is from Table 1. (d) Final mass ratio of adsorption to overlying water phase (P_{SO}), overlying water phase to pore water phase (P_{OC}), and and adsorption to pore water phase (P_{SC}).

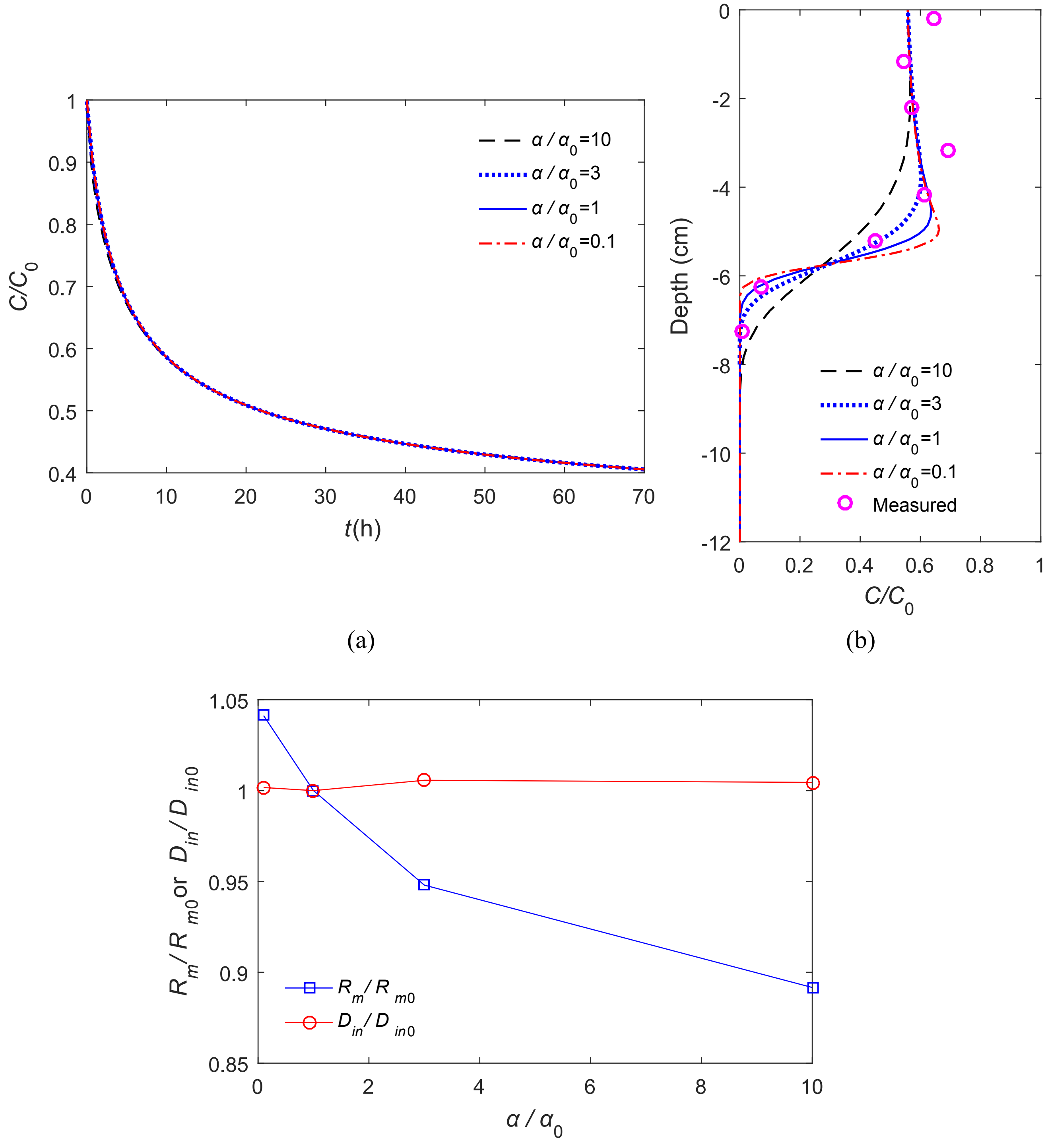

(a) (b)

(c)

Fig. 7. Effects of dispersivities (α). (a) Concentration in overlying water for different α. (b) Zn^{2+} concentration in the pore water at t = 797 min in profile N1. (c) Variation of R_m/R_{m0} and D_{in}/D_{in0}.

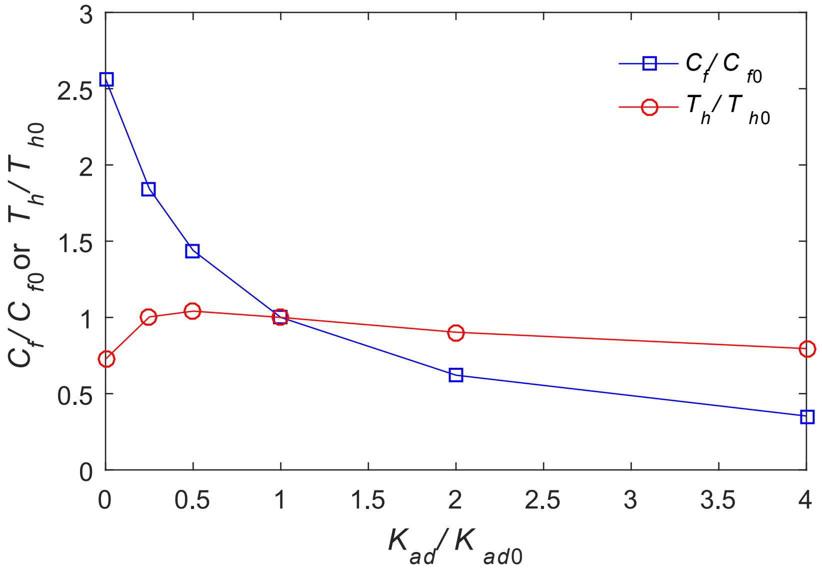

Fig. 8. Variation of the final stable concentration (C_f) and half concentration arrival time (T_h) with the equilibrium constant (K_{ad}).

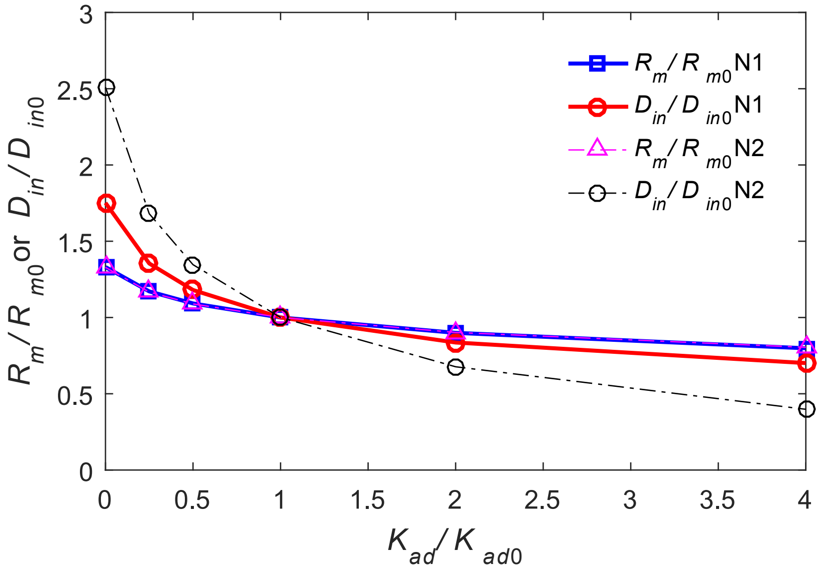

Fig. 9. Variation of the maximum-initial concentration ratio (R_m) and intrusion depth (D_{in}) with the equilibrium constant (K_{ad}) at 797 min.

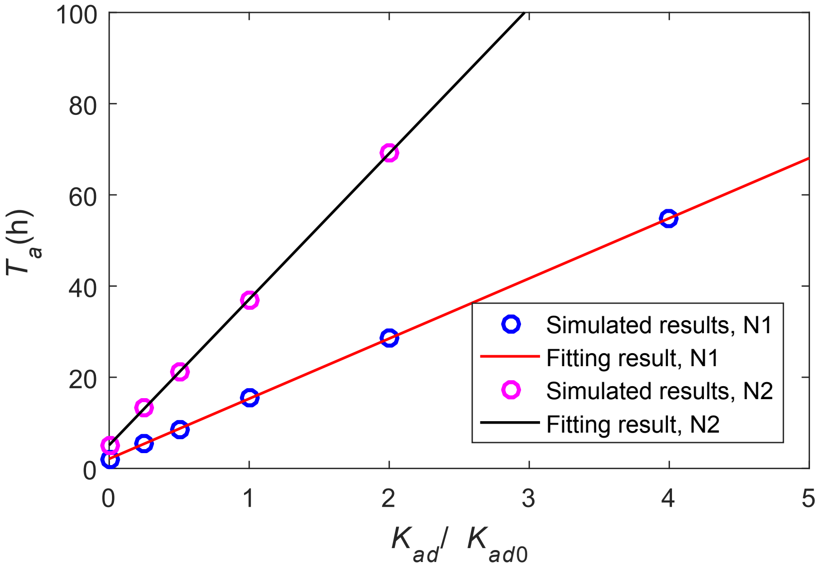

Fig. 10. Relationship between the arrival time at column N1 and K_{ad} / K_{ad0}. The circles represent the simulation results and the lines are linear fits. K_{ad0} is the fitted equilibrium constant based on measured data.

Table 1. Parameters for experiments and simulations.

Parameters	Values	Parameters	Values
Average flow rate of the overlying water (v)	12.78 cm s^{-1}	Porosity (θ)	0.33
Average depth of the overlying water (H)	8.22 cm	Water density (ρ)	1000 kg m^{-3}
Length of the bedform (L)	15.2 cm	Hydrodynamic viscosity coefficient (μ)	0.001 Pa s
Height of top of the bedforms (H_b), Fig. 1b	2 cm	Longitudinal dispersivities (α_L)	0.001 m
Length of the stoss side of the bedform (L_c)	11.4 cm	Transverse dispersivities (α_T)	0.0001 m
Minimum bedform height (H_s), Fig. 1b	12.0 cm	Effective molecular diffusion coefficient	10^{-9} m^2 s
Hydraulic conductivity (K)	8.83×10^{-4} m s^{-1}	Initial concentration of Zn^{2+} (C_0)	2.34×10^{-3} kg m^{-3}
Equilibrium constant for linear adsorption (K_{ad})	0.00142 m^3 kg^{-1}	Bulk density of sand bed (ρ_b)	1.454×10^3 kg m^{-3}

Supporting Information

Transport of zinc ions in the hyporheic zone: Experiments and simulations

Guangqiu Jin, Zhongtian Zhang, Ruzhong Li, Chen Chen, Hongwu Tang*, Ling Li, David Andrew Barry

S1 Mesh selection

In order to choose a suitable mesh for numerical simulation, four meshes with different grid densities were tested (Fig. S1a). The results show that different grid densities have little effect on the concentration variations in the overlying water (Fig. S1b). However, the pore water concentrations differ (Fig. S1c). For Meshes 1 and 2, the concentrations show irregular features, which are not noticeable for Meshes 3 and 4. Consequently, Mesh 3 was used subsequently.

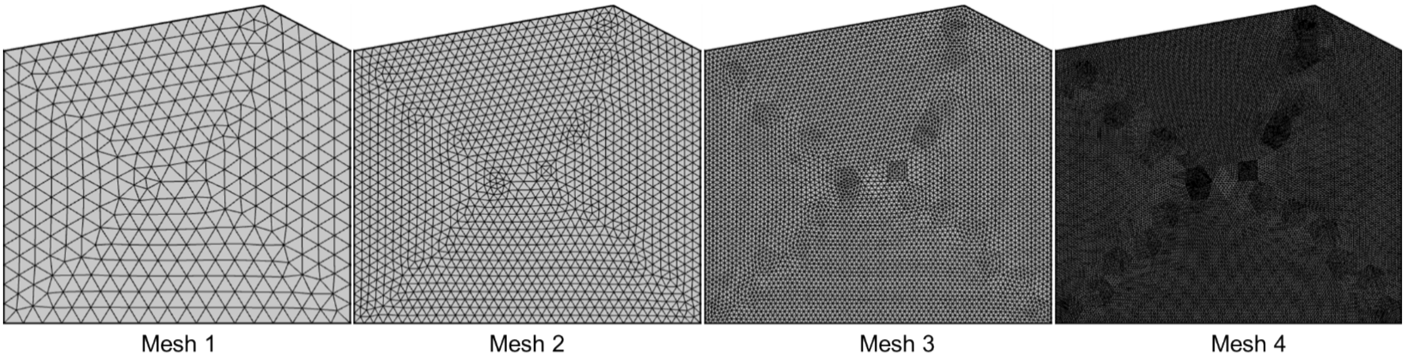

(a)

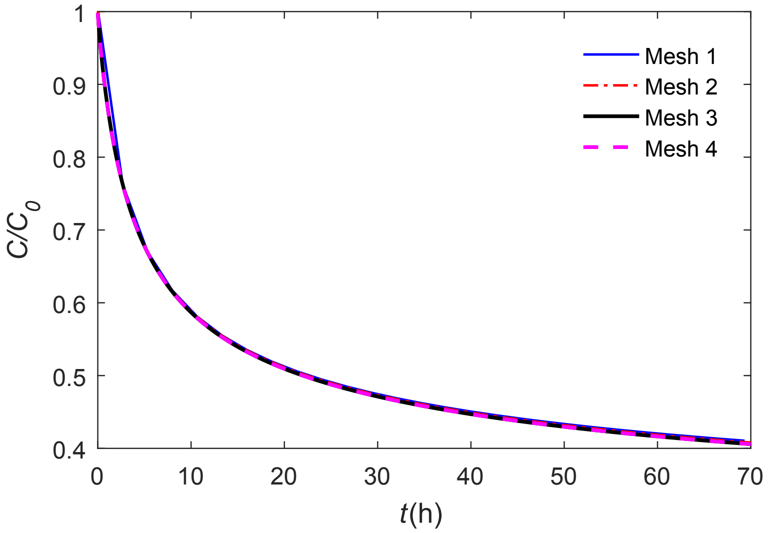

(b)

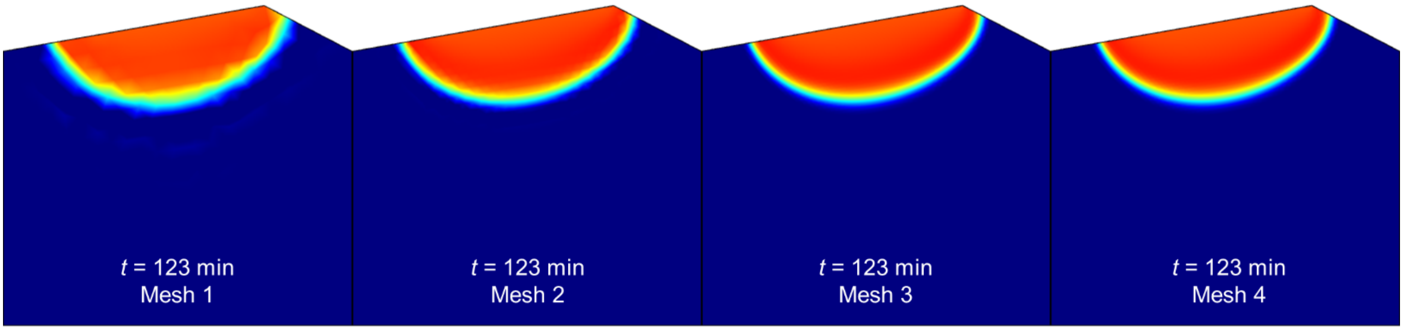

(c)

Fig. S1. (a) Different meshes tested. Meshes 1-4 contained, respectively, 697, 2788, 11152, 44608 grids. Concentration variations in the (b) overlying water and (c) pore water simulated by meshes computed for different meshes.

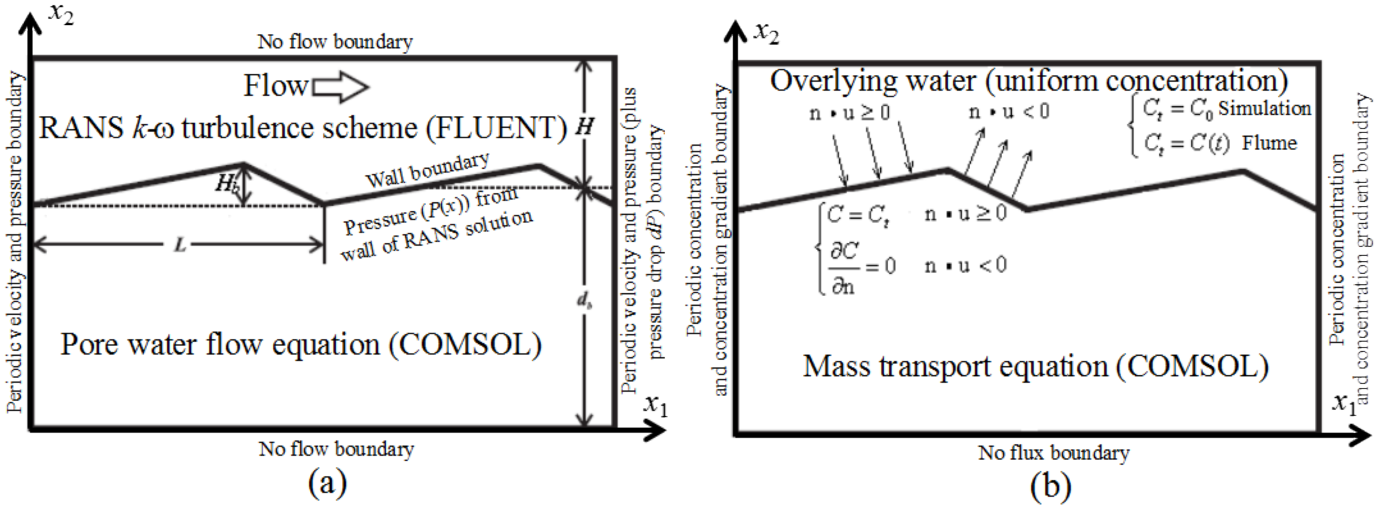

Fig. S2. Schematic of simulation domain and boundaries. (a) Water flow (overlying water and porewater flow). L, H, H_b and d_b are the bedform length, average water depth of the overlying water, bedform height and average depth of streambed, respectively. (b) Solute transport. A uniform concentration is assumed in the overlying water. For the solute released from streambed, the total quantity of solute in the overlying water and pore water is assumed to be constant over time in the flume experiment but the concentration in the overlying water is assumed to vary.

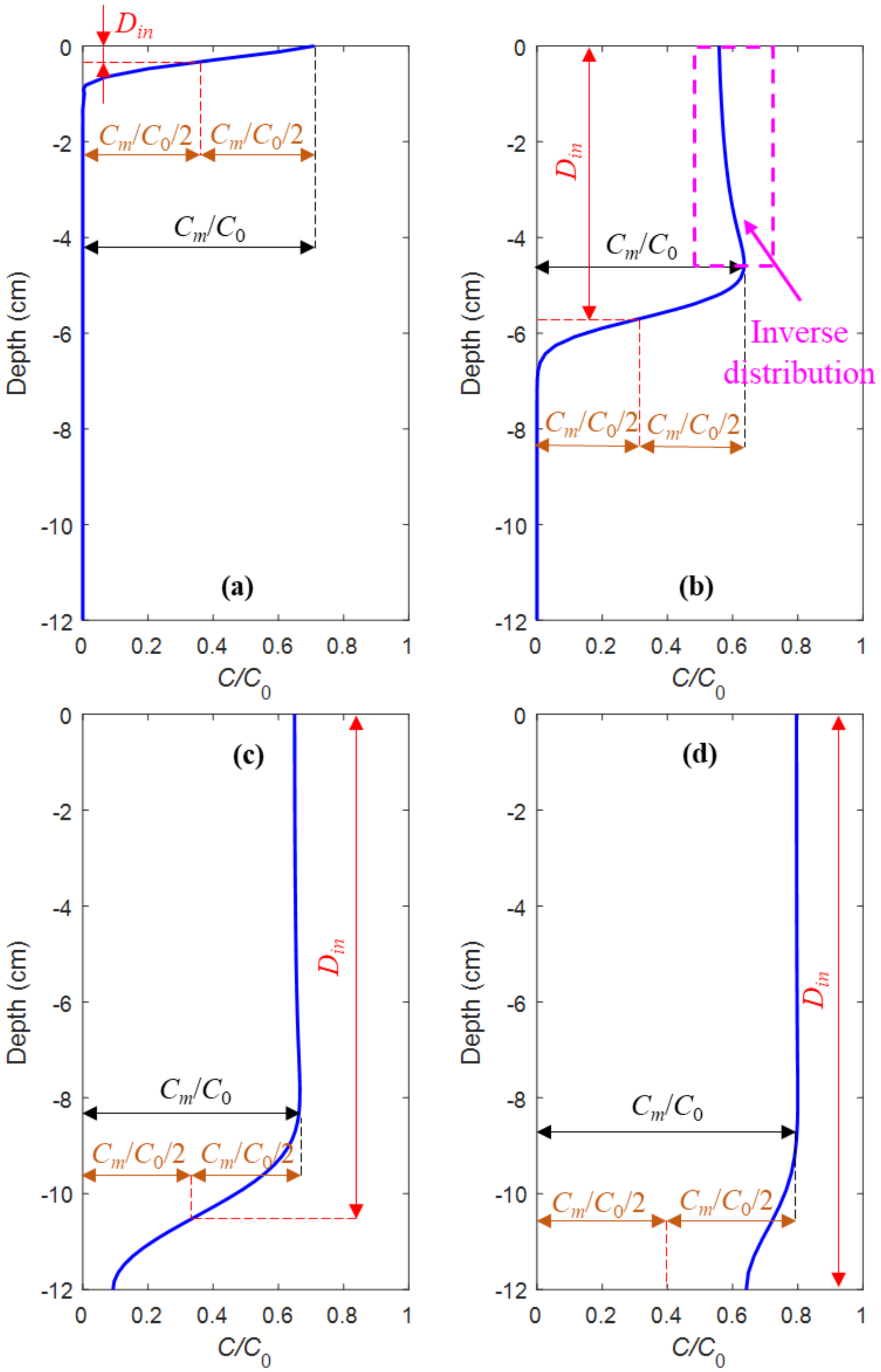

Fig. S3. Sketch for maximum-initial concentration ratio ($R_m = C_m/C_0$) and intrusion depth (D_{in}) in four different cases, and the curves in the figure do not represent real measured data. (a) The peak concentration for the intrusion line has not reached the profile. (b) The peak concentration for the intrusion line has reached the profile ahead of the front tip. (c) The solute has reached the bottom of the profile but the intrusion depth (D_{in}) has not reached the bottom; (d) The intrusion depth (D_{in}) has reached the bottom.

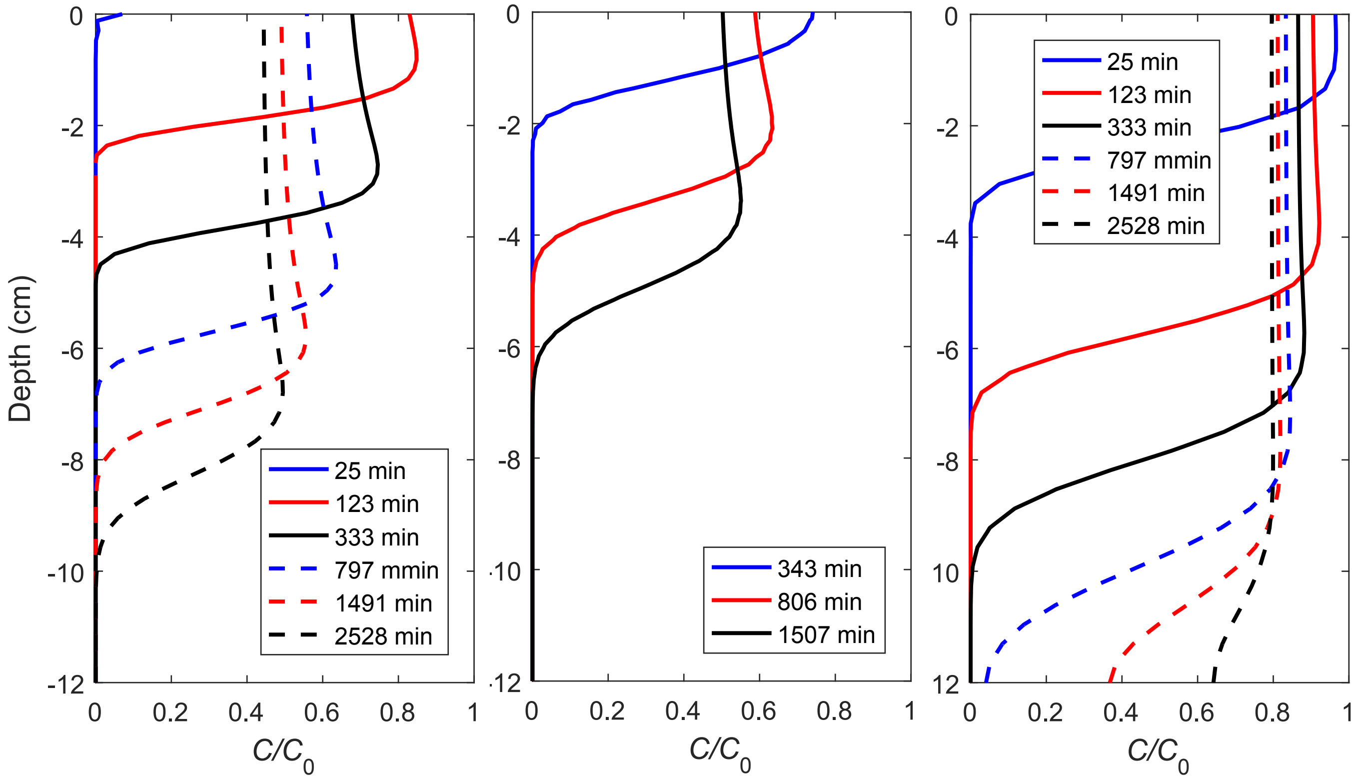

(a) (b) (c)

Fig. S4. Computed concentrations (a) at profile N1 for Zn^{2+}; (b) at profile N2 for Zn^{2+}; and (c) at profile N1 for NaCl.

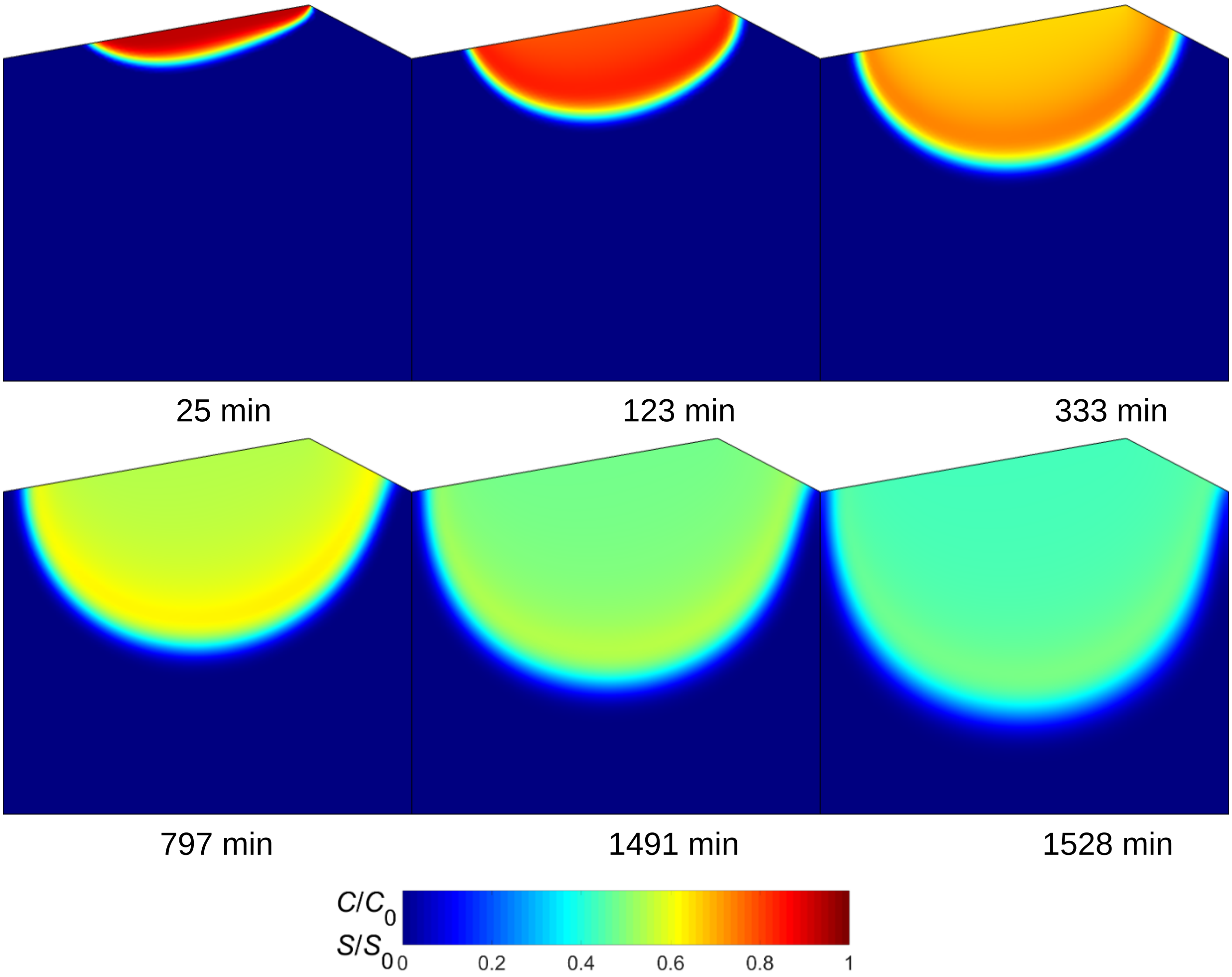

Fig. S5. Normalized concentrations of Zn^{2+} in pore water and adsorbed at different times. These results are for the linear adsorption isotherm (Eq. 3, 4), so the distributions of C/C_0 and S/S_0 are identical.

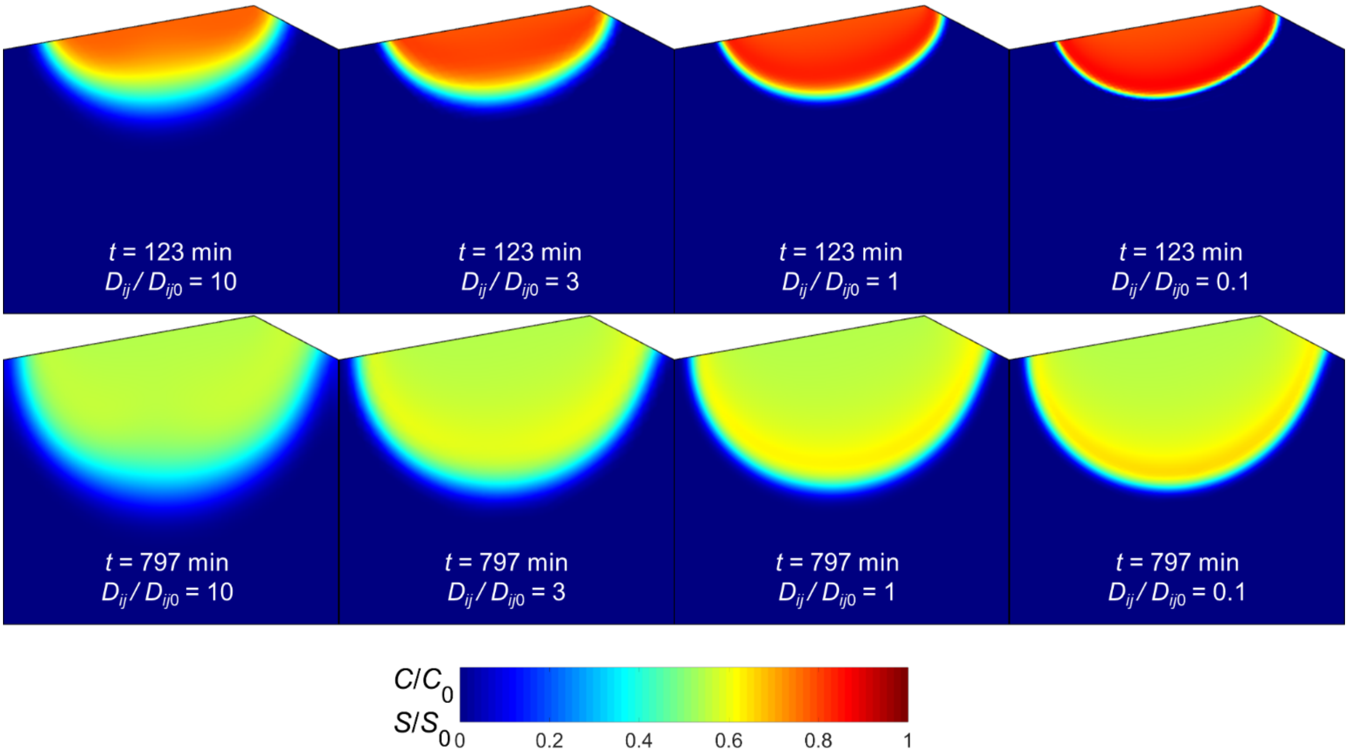

Fig. S6. Normalized concentrations in the bedform for different dispersion coefficients.

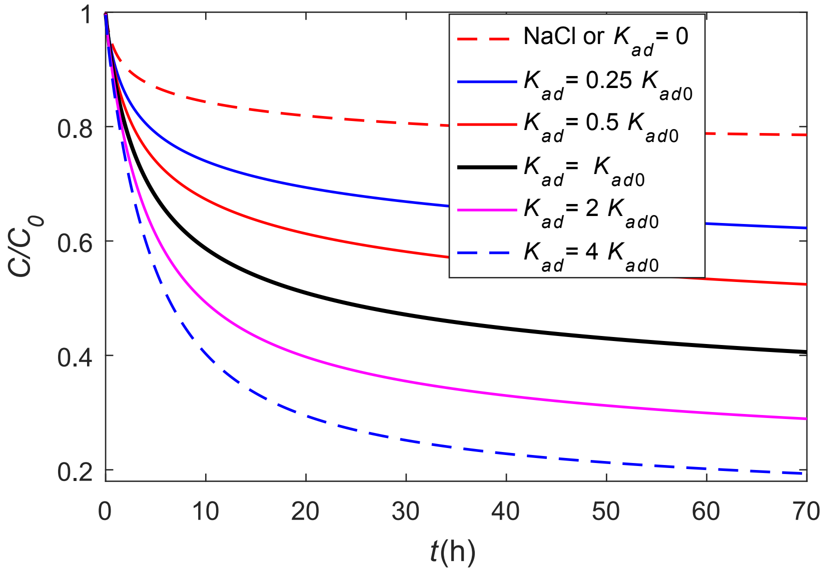

Fig. S7. Normalized concentration evolution in the overland water for different equilibrium constants.

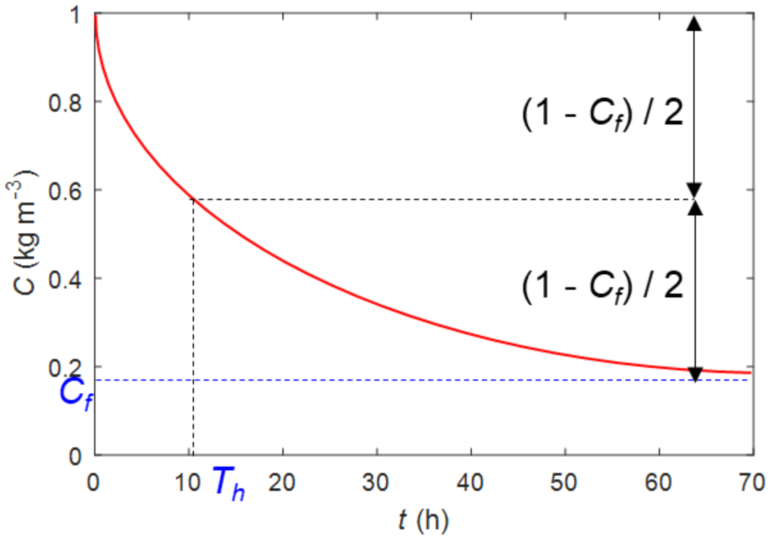

Fig. S8. Definition of final stable concentration (C_f) and half concentration arrival time (T_h).

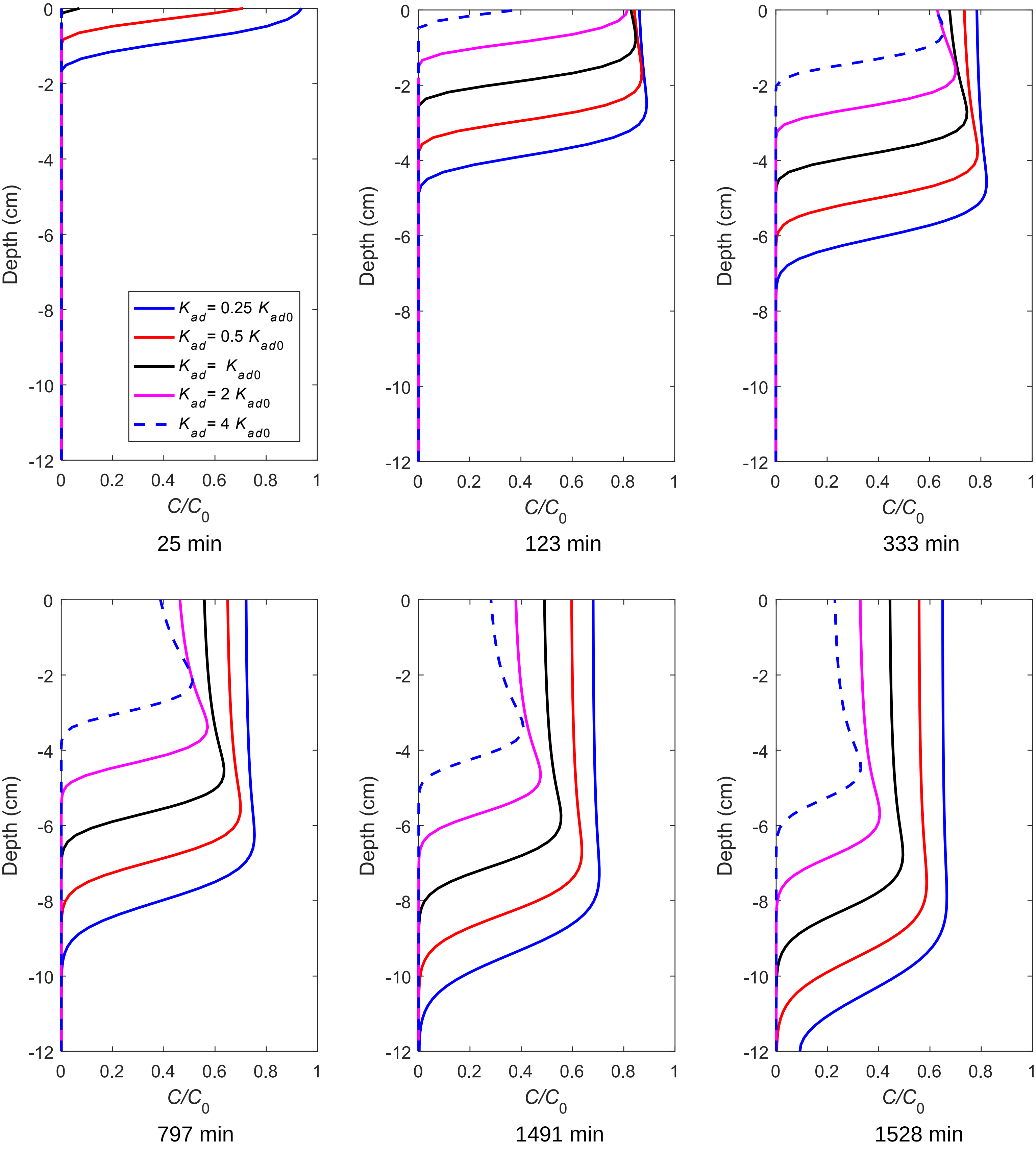

Fig. S9. Concentration variations in pore water at N1 for different equilibrium constants (K_{ad}).

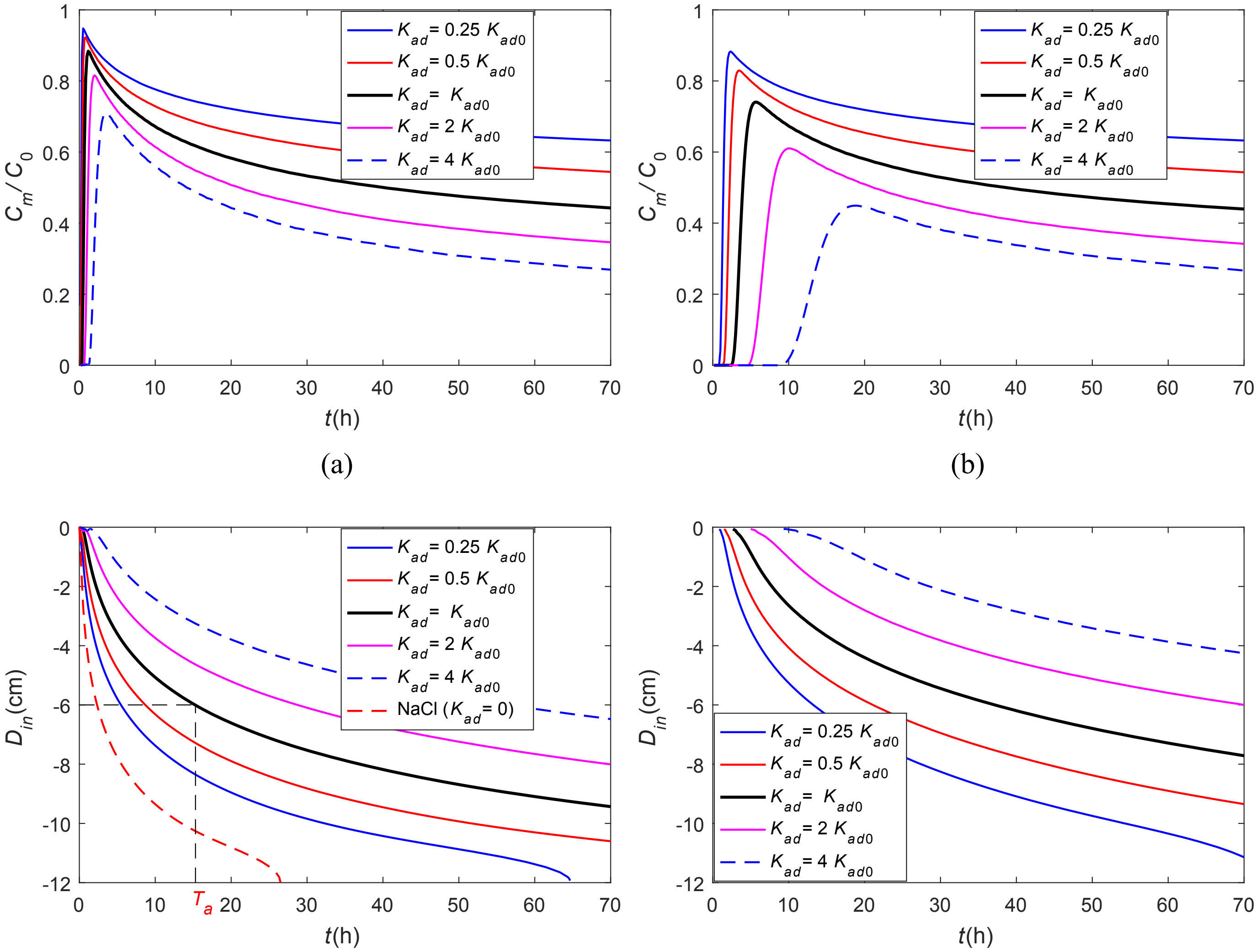

(a) (b)

(c) (d)

Fig. S10. Maximum intrusion concentration (C_m) and intrusion depth (D_{in}) for different equilibrium constants (K_{ad}) for different vertical profiles. (a) and (c) N1; (b) and (d) N2. K_{ad0} is the fitted equilibrium constant for measured data. T_a (h) is the arrival time when the D_{in} is -6 cm.